Comparison of two modelling strategies for 2D large-scale flood simulations

Susanna Dazzi, Iuliia Shustikova, Alessio Domeneghetti, Attilio Castellarin, Renato Vacondio

Comparison of two modelling strategies for 2D large-scale flood simulations

In: Environmental Modelling & Software, volume 146, 2021

Comparison of two modelling strategies for 2D large-scale flood simulations

Susanna Dazzi[a,*], Iuliia Shustikova[b,c], Alessio Domeneghetti[b], Attilio Castellarin[b], Renato Vacondio[a]

[a]*Department of Civil Engineering and Architecture, University of Parma, Viale Parco Area delle Scienze 181/A, 43124, Parma, Italy*
[b]*Department of Civil, Chemical, Environmental and Material Engineering, University of Bologna, Viale Risorgimento 2, 40136, Bologna, Italy*
[c]*Willis Towers Watson, 51 Lime Street, London, EC3M 7DQ, United Kingdom* (present address)
*corresponding author

E-mail addresses: S.D. (susanna.dazzi@unipr.it); I.S. (iuliia.shustikova@willistowerswatson.com); A.D. (alessio.domeneghetti@unibo.it); A.C. (attilio.castellarin@unibo.it); R.V. (renato.vacondio@unipr.it)

ABSTRACT

In this paper, two emerging strategies for the reduction of the computational time of 2D large-scale flood simulations are compared, with the aim of evaluating their strengths and limitations and of suggesting guidelines for their effective application. The analysis is based on two state-of-the-art raster flood models with different governing equations and parallelization strategies: PARFLOOD, a GPU-accelerated code that solves the fully dynamic shallow water equations, and LISFLOOD-FP, which combines a parallel implementation for CPU with simplified equations (local-inertial approximation). The results of two case studies (a river flood propagation, and a lowland inundation) suggest that, at coarse grid resolutions, the parallelized simplified model LISFLOOD-FP can represent a good alternative to fully dynamic models in terms of accuracy and runtime, while the GPU-parallel code PARFLOOD is more efficient in case of high-resolution simulations with millions of cells, despite the greater complexity of the numerical scheme.

KEYWORDS

2D inundation models; shallow water equations; local inertial approximation; model benchmarking; hydraulic simulations; parallel computations

1. Introduction

Floods have the potential to cause huge economic losses and casualties, and future projections on climate change and on the settlement of people and assets in flood-prone areas indicate that flood losses are expected to increase in the next decades (Winsemius et al., 2016; Dottori et al., 2018b).

For this reason, most countries are developing flood risk management strategies to prevent or mitigate the adverse impacts of floods on the communities (Klijn et al., 2008). These plans must be based on flood hazard and flood risk maps (de Moel et al., 2009), as demanded for example by the European legislation (European Commission, 2007). In this context, numerical models represent an essential tool for flood hazard assessment, even though the large number of available approaches (Teng et al., 2017) makes the selection of the most appropriate model for each application a non-trivial task.

For large-scale studies, simplified conceptual models (e.g. Lhomme et al., 2008; Nobre et al., 2016), also called "low-complexity" methods, are sometimes preferred over physically based approaches for flood mapping, especially for data-scarce regions (Samela et al., 2017; Tavares da Costa et al., 2020). Even though these methods are only based on geomorphological indicators (e.g. Nardi et al., 2006; Manfreda et al., 2014; Zheng et al., 2018; Tavares da Costa et al., 2019) or represent the underlying physical process of flooding in a very simplified way (e.g. Dottori et al., 2018a; Teng et al., 2019), they are able to provide inundation extents that are reasonably comparable to those obtained from hydraulic studies (Falter et al., 2013; Afshari et al., 2018) in a fraction of the computational time (Néelz & Pender, 2013). However, only physically based numerical models can provide detailed flow data (Néelz & Pender, 2013; Wing et al., 2019a), i.e. all flow variables (depths and velocities, but also derived physical quantity, e.g. Froude number, hydraulic thrust, etc.) at all locations, and also their variation in time (i.e. flow dynamics, including the flood arrival time). All these data are required not only for flood hazard assessment, but also for other applications, such as the evaluation of flood protection strategies (e.g. Luke et al., 2015; Schubert et al., 2017), and emergency planning and civil protection activities (e.g. Arrighi et al., 2019; Amadio et al., 2019; Ferrari et al., 2020).

One-dimensional (1D) hydrodynamic models (e.g. Brunner, 2016; DHI, 2015) are still widely employed for river studies (e.g. Horritt & Bates, 2002; Paz et al., 2010; Schumann et al., 2010; Ali et al., 2015). Their computational requirement is usually limited, but these models may cause some inaccuracies in representing the actual flow field outside the main channel, i.e. when floodplains are inundated or when the design return period of structural flood defense systems (e.g. river levees) is exceeded and lowland areas are flooded. For these applications, the 1D model for the river is often combined with a two-dimensional (2D) model for the floodplains (Tayefi et al., 2007; Bladé et al., 2012; Morales-Hernández et al., 2013; Ahmadian et al., 2015), especially when levee-breach inundations need to be modelled (Vorogushyn et al., 2010; Pinter et al., 2016; D'Oria et al., 2019). Alternatively, fully 2D models (e.g. Galland et al., 1991; Alcrudo & Garcia-Navarro, 1993; Aureli et al., 2008; Sanders et al., 2010; Bates et al., 2010) can be used for simulating the whole domain.

Until recently, the limiting factors for 2D models were the common unavailability of Digital Terrain Models (DTMs) for geographically large areas and, most prominently, the insufficient computational power to run fully 2D simulations on large domains. Nevertheless, high-resolution terrain data are

now increasingly available thanks to remote sensing techniques. In particular, airborne Light Detection and Ranging (LiDAR) surveys can provide DTMs with spatial resolution up to 0.5-1 m and vertical accuracy between 0.05 and 0.15 m (Di Baldassarre & Uhlenbrook, 2012), and now represent the main topographic source for hydraulic models (Marks & Bates, 2000; Sanders, 2007). In data-sparse regions, digital elevation models with lower resolution and accuracy can be obtained from open-access global data sets (e.g. Sanders, 2007; Yan et al., 2013; Courty et al., 2019).

As regards the prohibitive runtimes of 2D simulations, different strategies have been adopted for speeding up the computations for large-scale applications. First, low-resolution meshes, obtained from the aggregation of the original LiDAR data, are often used. Typical cell sizes are in the order of 25-100 m (Aureli & Mignosa, 2005; Vorogushyn et al., 2010; Falter et al., 2013; Jarihani et al., 2015; Morsy et al., 2018), though some studies underline the importance of including relevant terrain elements (e.g. levees, embankments, channels, etc.) to predict the flooding dynamics more accurately (e.g. Vacondio et al., 2016; Wing et al., 2019b). Automatic tools for the extraction of terrain features (e.g. Sofia et al., 2014; Sangiretti et al., 2016) or sub-grid models (e.g. Yu & Lane, 2006; Neal et al., 2012a) can be exploited to counterbalance the loss of topographic details in low-resolution meshes.

Another approach developed for reducing the computational burden of 2D models is the simplification of the governing equations. Free-surface flows are described by depth-averaged mass and momentum conservation laws, the Shallow Water Equations (SWEs) (Toro, 2001). Neglecting one or more terms in the momentum equation leads to models with decreasing levels of complexity; in particular, the diffusive formulation (Cunge et al., 1980) cancels both inertial terms (local and convective acceleration), and has the advantage of allowing simple solution and implementation compared to a “fully dynamic” model (Prestininzi, 2008; Aricò et al., 2011). However, some limitations have been identified: applicability only in cases with slowly varying flow (Néelz & Pender, 2013); difficulty in simulating processes where inertia plays a key role, e.g. flow over a bump (Neal et al., 2012b), or where highly unsteady and transcritical flows are expected, e.g. dam-breaks and urban inundations (Hunter et al., 2008; Costabile et al., 2017, 2020a); and requirement of a small time step for stability (Hunter et al., 2008; Bates et al., 2010). For these reasons, less simplified formulations were later proposed: the local-inertial approximation (Aronica et al., 1998; Bates et al., 2010; Martins et al., 2015) only neglects the convective acceleration term in the momentum equation and allows a larger time step for stability compared to a diffusive model, while maintaining its numerical simplicity (Bates et al., 2010). This kind of model is widely used for large-scale studies (Neal et al., 2012a; Falter et al., 2013; Savage et al., 2016a; Wing et al., 2017), though some problems are reported for wet/dry fronts (Cozzolino et al., 2019), for low friction values and high Froude numbers (Bates et al., 2010; De Almeida & Bates, 2013), and for processes involving hydraulic jumps, rapidly varying flows, etc. (Neal et al., 2012b). In all these cases, models based on the fully dynamic SWEs are necessary. These latter models may be characterized by different numerical discretization methods (finite

difference, finite volumes, finite elements; implicit or explicit) and grid types (structured, unstructured, flexible) (Teng et al., 2017), but the importance of using shock-capturing schemes is widely acknowledged (Néelz & Pender, 2013; Kvočka et al., 2015).

Besides (or in addition to) simplifying the governing equations or using coarse meshes, the best strategy for reducing the computational burden is undoubtedly the use of parallelized codes, which can exploit multi-core processors, clusters for High Performance Computing (HPC), or Graphic Processing Units (GPU) devices. Examples of different parallelization techniques applied to 2D hydraulic models can be found in Neal et al. (2009, 2010), Sanders et al. (2010, 2019), Lacasta et al. (2014), Vacondio et al. (2014), and Morsy et al. (2018). The continuous improvement in computer hardware and the increasing trend in accessibility to HPC facilities or cloud computing services make the use of large-scale fully 2D models much more affordable nowadays.

In this context, benchmarking studies are becoming crucial to provide insight into the strengths and limitations of the available models and to guide practitioners into the choice of the most appropriate approach. Previous works on the comparison of 2D models mainly focused on synthetic cases or small-scale applications (e.g. Neal et al., 2012b; Néelz & Pender, 2013; Willis et al., 2019), while more comprehensive analyses were carried out for urban flooding (Hunter et al., 2008; Costabile et al., 2020a) and rainfall-runoff modelling (e.g. Cea et al., 2010; Costabile et al., 2012, 2020b; Caviedes-Voullième et al., 2020). However, studies on highly detailed large-scale flood modelling using fully 2D codes are limited.

In this work, we evaluate the efficiency and accuracy of 2D large-scale simulations based on high-resolution LiDAR terrain data. In order to meet the modern tendencies of hydraulic modelling, we compare the capabilities of two state-of-the-art raster flood models, namely LISFLOOD-FP (Bates et al., 2010) and PARFLOOD (Vacondio et al., 2014), which are characterized by different governing equations, numerical schematizations, and parallelization strategies. In particular, LISFLOOD-FP exploits the local-inertial approximation for simplifying the numerical scheme and a shared-memory parallel implementation for CPU, while PARFLOOD is a GPU-accelerated code that solves the fully dynamic SWEs with an accurate shock-capturing scheme. The comparison is based on two real case studies, which were identified as suitable for both models (i.e. we deliberately excluded applications outside the range of applicability of simplified equations). The paper is aimed at outlining the main differences between the two models, discussing factors influencing their accuracy and runtime (e.g. grid resolution), and providing potential users with guidelines on the most viable and fruitful implementation strategies and settings.

The paper is structured as follows. We first briefly describe the two models, and discuss their similarities and differences (Section 2). Then, the two test cases and the model setup are presented (Section 3). The main simulation results are reported and discussed in Section 4, while conclusions are drawn in the last Section.

2. Model description

2.1 LISFLOOD-FP

LISFLOOD-FP is an inundation model that has been developed for research purposes at the University of Bristol (United Kingdom). It is specifically designed for large-scale applications and has been tested on various scales, including the continental and global scales (Savage et al., 2016b; Schumann et al., 2016). In recent years, the code has been updated and the current version (and the version used in this paper) applies the local inertial formulation of the SWEs (Bates et al., 2010). Such simplification allows for numerically stable solutions for subcritical flow conditions. The 2D model (used in this work) operates on a staggered Cartesian grid and applies an explicit finite difference scheme. The unit flow *q* between two cells is calculated by the following form of momentum equation:

$$q_{t+\Delta t} = \frac{q_t - g h_t \Delta t \frac{\Delta(h_t + z)}{\Delta x}}{1 + g h_t \Delta t n^2 q_t h_t^{-10/3}} \quad (1)$$

where *t* and *t*+Δ*t* indicate the current and next time step, respectively, *g* is the acceleration due to the gravity, *h* is the depth, *n* is Manning's roughness coefficient, Δ*x* is the cell resolution, *z* is the cell elevation, Δ*t* is the time step, and h_t is the difference between highest bed elevation and highest water surface elevation between two cells. The equation is coupled in *x* and *y* direction (four-directional), and then the continuity equation is used to update the water depth at each time step:

$$\frac{\Delta h^{i,j}}{\Delta t} = \frac{q_x^{i-1,j} - q_x^{i,j} + q_y^{i,j-1} - q_y^{i,j}}{\Delta x} \quad (2)$$

where *i* and *j* are the coordinates of a cell (Coulthard et al., 2013).

The full functionality of the code includes a sub-grid version (1D representation of the channel flow, not used herein) and may include rainfall, evaporation, runoff grid, as well as levee breach and dam-break sub-routines (Shustikova et al., 2020). Moreover, it allows to count for certain hydraulic structures. For more details, the interested readers are referred to the LISFLOOD-FP user manual (Bates et al., 2013). The code is parallelized and can be run on multiple cores on shared-memory systems (Neal et al., 2010).

The stability of the model is secured by the adaptive time step, which is derived from the Courant-Friedrichs-Lewy (CFL) condition and described in Bates et al. (2010). The time step for solution updating is calculated in the code as:

$$\Delta t = \alpha \frac{\Delta x}{\sqrt{g h_{max}}} \quad (3)$$

where α is a coefficient ranging from 0.2 to 0.7, which ensures the numerical stability for floodplain flows (Coulthard et al., 2013). In this work, the default value (i.e. 0.7) was adopted.

2.2 PARFLOOD

PARFLOOD (Vacondio et al., 2014, 2017), a research code developed at the University of Parma (Italy), exploits an explicit Finite Volume (FV) scheme to solve the complete 2D-SWE, written in conservative form (Toro, 2001):

$$\frac{\partial \mathbf{U}}{\partial t}+\frac{\partial \mathbf{F}}{\partial x}+\frac{\partial \mathbf{G}}{\partial y}=\mathbf{S}_0+\mathbf{S}_f \tag{4}$$

where the vector of conserved variables **U**, the fluxes in the *x*- and *y*-directions **F** and **G**, and the bed and friction slope source terms $\mathbf{S}_0$ and $\mathbf{S}_f$ are expressed using the well-balanced formulation of Liang & Marche (2009):

$$\begin{gathered}\mathbf{U}=[\eta;uh;vh]^T,\mathbf{F}=\left[uh;u^2h+\frac{1}{2}g(\eta^2-2\eta z);uvh\right]^T,\mathbf{G}=\left[vh;uvh;v^2h+\frac{1}{2}g(\eta^2-2\eta z)\right]^T,\\ \mathbf{S}_0=\left[0;-g\eta\frac{\partial z}{\partial x};-g\eta\frac{\partial z}{\partial y}\right]^T,\mathbf{S}_f=\left[0;-gh\frac{n^2u\sqrt{u^2+v^2}}{h^{4/3}};-gh\frac{n^2v\sqrt{u^2+v^2}}{h^{4/3}}\right]^T\end{gathered} \tag{5}$$

in which $\eta = h+z$ is the water surface elevation relative to the mean sea level (the ground elevation z is fixed), and u and v are the velocity components along x and y, respectively.

The partial differential equations (Eq. 4) are solved on a structured grid using a FV scheme that is explicit and second-order accurate in space and time, thanks to a depth-positive MUSCL reconstruction (Toro, 2001), and to the adoption of the second-order Runge-Kutta method to advance the solution in time:

$$\mathbf{U}_{i,j}^{t+\Delta t}=\mathbf{U}_{i,j}^{t}+\frac{1}{2}\Delta t\left[\mathbf{D}_i\left(\mathbf{U}_{i,j}^{t}\right)+\mathbf{D}_i\left(\mathbf{U}_{i,j}^{t+\Delta t/2}\right)\right] \tag{6}$$

where $\mathbf{U}_{i,j}^{t+\Delta t/2}$ is evaluated as follows:

$$\mathbf{U}_{i,j}^{t+\Delta t/2}=\mathbf{U}_{i,j}^{t}+\Delta t\mathbf{D}_i\left(\mathbf{U}_{i,j}^{t}\right) \tag{7}$$

while the operator $\mathbf{D}_i(\mathbf{U}_{i,j})$ is defined as:

$$\mathbf{D}_i\left(\mathbf{U}_{i,j}^{t}\right)=-\frac{\mathbf{F}_{i+\frac{1}{2},j}-\mathbf{F}_{i-\frac{1}{2},j}}{\Delta x}-\frac{\mathbf{G}_{i,j+\frac{1}{2}}-\mathbf{G}_{i,j-\frac{1}{2}}}{\Delta y}+S_0+S_f \tag{8}$$

where Δx and Δy are the grid sizes in the x and y directions, respectively, and the time step Δt is calculated according to the CFL stability condition (e.g. Toro, 2001):

$$\Delta t=\frac{1}{2}Cr\ \min\left(\frac{\Delta x}{|u|+\sqrt{gh}},\frac{\Delta y}{|v|+\sqrt{gh}}\right) \tag{9}$$

where Cr is the Courant number (<1). In this work, Cr was assumed equal to 0.8.

In Eq. 8, fluxes are computed using the HLLC approximate Riemann solver (Toro, 2001), the bed slope source term is discretized with a centered approximation, while for the friction source term an implicit formulation is adopted. Moreover, in order to avoid non-physical flow velocities at the wet/dry front, the correction proposed by Kurganov & Petrova (2007) is introduced. The domain can be discretized adopting either a Cartesian or a non-uniform structured grid, named Block Uniform Quadtree (BUQ) grid (Vacondio et al., 2017), but in this work only uniform meshes are used for

compatibility with LISFLOOD-FP. A first-order accurate version of the code is also available, but not used herein.

In order to reduce the high computational cost of this accurate and robust numerical scheme, the code is efficiently implemented in C++ and Compute Unified Device Architecture (CUDA) languages. Basically, the CUDA framework, introduced by NVIDIA™, allows offloading the intensive computations on the GPU and exploiting its intrinsic parallelization capabilities, while the CPU only controls the execution flow and the time advancement of the simulation. For more details, the reader is referred to Vacondio et al. (2014). The model also features extensions to include levee/dam breaches (Dazzi et al., 2019), and hydraulic structures (Dazzi et al., 2020). Previous applications to real flood simulations showed the good computational performance of the code, even for domains with several million cells (Dazzi et al., 2018; Ferrari et al., 2020).

2.3 Comparison of model features

Table 1 summarizes the main features of the two models used in this work. Please notice that LISFLOOD-FP is a package including different solvers, but here we only consider the “acceleration” version of the model, which is widely used in large-scale studies.

As explained above, the main difference between the two models is represented by the governing equations and numerical scheme adopted. On the other hand, both codes rely on an explicit solution method and on an adaptive time step for updating the flow variables, though the time step is restricted by a different version of the CFL stability condition (Eq. 3 for LISFLOOD-FP; Eq. 9 for PARFLOOD). Both models perform computations on a raster-based grid, even if PARFLOOD also supports non-uniform structured grids (Vacondio et al., 2017). The grid preparation and the visualization of results can be performed directly using any GIS software, which is convenient considering that these research codes are not provided with a Graphical User Interface (GUI); in fact, simulations can only be launched from the command line.

Simulation results include the maps of water depths and velocities at predefined time intervals, and final maps with maxima or other useful information (e.g. arrival times). However, the two models inherently differ in the way velocity is computed. PARFLOOD updates cell-centered values for the unit discharges, from which the velocity magnitude can be directly obtained for each cell. LISFLOOD-FP adopts a staggered grid, hence unit discharge values are evaluated at cell interfaces in the *x*- and *y*-directions; the velocity magnitude *V* in each cell is then retrieved as in Eq. 10:

$$V_{i,j} = \left(\left[max\left(V_{i-\frac{1}{2},j}, V_{i+\frac{1}{2},j} \right) \right]^2 + \left[max\left(V_{i,j-\frac{1}{2}}, V_{i,j+\frac{1}{2}} \right) \right]^2 \right)^{0.5} \quad (10)$$

Another important difference between the two models lies in their parallel implementation. The Open multiprocessing (OpenMP) Application Programming Interface is adopted to parallelize computations in LISFLOOD-FP (Neal et al., 2009) taking advantage of shared-memory multiprocessors, if available on the host machine. Conversely, the PARFLOOD model exploits

acceleration on a GPU device thanks to its CUDA implementation. For this reason, hardware requirements are more restrictive for the latter model, since a machine equipped with an NVIDIA GPU is mandatory. The fact that the two codes run on different types of hardware makes the direct comparison on the same machine impossible. The runtimes reported in this work are obtained using the following hardware, unless otherwise specified:

- LISFLOOD-FP: 2 CPUs having 20 real cores and hyperthreading 40 cores;
- PARFLOOD: NVIDIA Tesla® P100 (12 GB memory, release year 2016).

All simulations are run using double precision.

Table 1. Summary of main features of LISFLOOD-FP and PARFOOD. Italics is used to indicate features that are the same for both models.

Model features	**LISFLOOD-FP**	**PARFLOOD**
Governing equations	SWE with local-inertial approximation (other solvers available)	Fully dynamic SWE
Numerical scheme	Finite difference	Finite volume (first- or second-order accurate)
Time discretization	*Explicit*	*Explicit*
Time step for stability	Adaptive; restricted by Eq. 3	Adaptive; restricted by Eq. 9
Cell updating	*Only wet cells*	*Only wet cells*
Grid type	*Structured*	*Structured* (Cartesian or BUQ)
Parallelization	OpenMP	CUDA/C++ for GPU
Hardware requirements	Workstation/cluster with one or more CPUs	Workstation/cluster with NVIDIA GPU that supports CUDA
Floating point precision	*Single/double*	*Single/double*
GUI	*No*	*No*
Language	C++	CUDA, C++
Operating system	Windows, Linux	Linux
Code availability	Research code, freely available for research purposes	Research code, currently available only for scientific collaboration
Developed by	University of Bristol (UK)	University of Parma (Italy)
Main references	Bates et al. (2010), Neal et al. (2012)	Vacondio et al. (2014, 2017)

3. Case studies and model set-up

In this Section, the two case studies selected for the models' comparison are described. As already mentioned, we focused on typical applications for which the choice of either fully dynamic or simplified models may be considered suitable, i.e. gradually varied flows. The first test case concerns the propagation of a severe flood wave in a large river (Po River, Italy), where a fully 2D model is appropriate to predict the inundation of protected floodplains. The second test case is an inundation event that followed the opening of a sudden levee breach on the Secchia River (Italy): the outflows propagated over an initially dry lowland area, characterized by anthropogenic terrain features (a complex network of irrigation canals and embankments). Local hydraulic shocks or critical flows, which can occur in this complex test case, are not expected to dominate the overall phenomenon, thus this flood event can still be described well by the local-inertial formulation of LISFLOOD-FP (Hunter et al., 2008; Neal et al., 2012b).

3.1 Po River

We first analyse a well-documented flooding event, which occurred on the Po River (Italy) in October 2000. This flood is considered as one of most severe in the recent decades. Uncommonly heavy rainfalls extended all over the upstream part of the basin, where the flood caused several deaths and severe damage (Cassardo et al., 2001). In the current study, however, we limit the analysis to the mid-lower portion of the Po River (Figure 1), where the flood was contained by the main embankments (designed to protect against a 1 in 200 years' flood). During the event, the floodplains behind minor embankments (with a design return period of 50 years) were also activated. In the recent past, this case study was used to setup a quasi-2D model of the Po River for flood risk mitigation purposes (Castellarin et al., 2011; Domeneghetti et al., 2015).

The study area (more than 800 km^2 wide) covers the 330 km-long reach of the Po River between Ponte Becca and Serravalle (Figure 1). The domain includes the compartments (i.e. defended floodplains) inside the main levees, and a 100 m-wide buffer area outside the embankment. Figure 1 also shows a detail of the extensive system of main and minor embankments with different design return periods.

The 2 m-resolution DTM of the area was obtained from LiDAR surveys performed in years 2004-2005. The bathymetric data were collected using multi-beam sonars during approximately same period (Castellarin et al., 2011). The DTM used in the study represents bare earth terrain, cleared from trees and buildings, with vertical accuracy of about ±0.15 m. We aggregated the 2 m-terrain data into 30, 50 and 100 m raster grids, using the pixels' mean value. The resulting meshes included $9 \cdot 10^5$, $3 \cdot 10^5$, and $9 \cdot 10^4$ cells, respectively. We also manually "burnt" in the actual height of main and minor embankments. Since the models adopt the same cell size as the input data, different resolutions will have an impact on the storage capacity of the floodplain. For example, a DTM with

100 m resolution will result in 100 m-wide levees, which in turn reduce the potential volume between the main embankments.

The upstream boundary condition on the Po River was set at Ponte Becca, and the inflow from the main tributaries (Trebbia, Lambro, Taro and Adda) was also included. These hydrographs were obtained from the river gauges' measurements. A free outflow boundary condition was set 40 km downstream from Pontelagoscuro gauging station (Figure 1), just upstream of the Po Delta. The simulation ends after 191 h of physical time.

Model calibration was performed with reference to the maximum water levels along the reach. Altogether, 171 watermark records, taken from the official report delivered by the Po River Basin Authority, were available. The vertical errors in such measurements are known to be up to 0.5 m (Dottori et al., 2013). The calibration was performed separately for each numerical model, considering the configuration with 30 m resolution. The initial distribution of spatially-variable roughness coefficients, divided in two main classes (channel and floodplain), was taken from the work done by Domeneghetti et al. (2015). Manning's coefficients were manually varied trying to minimize the Root Mean Square Error (RMSE) of simulated and observed maximum water surface elevations on the 171 water marks. Because the flooding extent was outlined by the main embankments, we additionally visually inspected the levees to verify the presence of overflows. If some non-negligible overflows occurred during the simulation, we would disqualify the configuration. We adopted the same set of roughness coefficients calibrated for the 30 m DTM also for 50 and 100 m configurations: for these latter simulations, we are mainly interested in a comparison between the two models' runtimes, hence a specific calibration was not carried out.

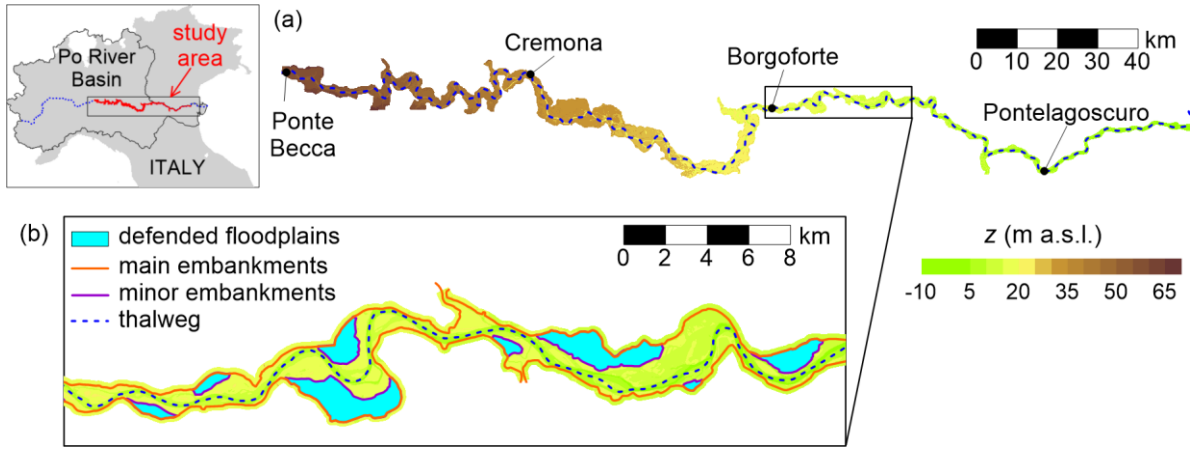

Figure 1. Study area for the Po River case study: (a) DTM, and (b) example of floodplains and embankments in a sub-portion of the domain.

3.2 Secchia River

The second case study chosen for the comparison is the levee-breach-induced inundation that occurred in 2014 on the Secchia River, a tributary of the Po River (the study area is shown in Figure

2a). This well-documented event (D'Alpaos et al., 2014) has been used in previous studies for the validation of numerical models (Vacondio et al., 2016), for flood loss models (Carisi et al., 2018), and for the comparison of existing hydraulic models (Shustikova et al., 2019).

During the flood event of 19 January 2014, the right embankment of the Secchia River collapsed: post-event investigations ascribed this failure to the dens of burrowing animals that most likely contributed to weakening the levee (Orlandini et al., 2015). The breach final width was approximately 80 m, and the overall flooded volume reached almost 40 Mm^3. In 48 hours, the inundation affected roughly 50 km^2 of lowland area in the municipalities of Modena, Bastiglia and Bomporto, and caused about 400 million Euro of economic losses, one casualty, and the displacement of thousands of people (Vacondio et al., 2016). The flood propagation was strongly influenced by terrain features like road embankments and minor-channel levees.

The study area is roughly 170 km^2 wide and is fully covered by a DTM of 1 m resolution, obtained from a LiDAR survey (Figure 2a). Terrain data were then down-sampled to create grids with 5, 25, and 50 m resolution, by taking the pixels' mean value. However, the crest elevation of artificial embankments, obtained from the original LiDAR DTM, was enforced in low-resolution cells crossed by these elements, which can be thus correctly represented even adopting coarse meshes. The resulting grids consist of roughly $6.8 \cdot 10^6$, $3 \cdot 10^5$, and $8 \cdot 10^4$ cells for 5 m, 25 m, and 50 m resolutions, respectively.

The land-use of the area was analyzed on orthophotographs (available from the Geoportal of Emilia-Romagna Region) in order to define spatially-variable values for the roughness coefficient. Two main classes were identified: urban areas (including both residential and industrial land use), and rural areas (the remaining part of the domain, which is mainly covered by agricultural fields). Based on the previous studies carried out by Vacondio et al. (2016) on the same area, the value 0.143 $m^{1/3}s$ for Manning's coefficient was adopted for the urban areas (outlined in Figure 2a), while three different values were investigated for the rural areas (in particular 0.03, 0.05, and 0.07 $m^{-1/3}s$). These values are in line with indications from the literature for floodplains (Chow et al., 1988). Please notice that a detailed representation of buildings in the urban areas would require a higher resolution (1-2 m, i.e. at least three cells across each street, according to Gallegos et al., 2009), while the strategy of imposing a high resistance in the urban area is commonly adopted for large-scale modelling.

The discharge hydrograph flowing through the breach (Figure 2b) was obtained from previous works (Vacondio et al., 2016), and imposed as inflow boundary condition at the breach location (the river flood was therefore not included in the simulation). The simulations cover 48 hours after the breach opening.

Available data for this event include the flood arrival times at two selected locations in the study area, namely the urban areas of Bastiglia and Bomporto, and 46 high watermarks at certain points, collected during post-event surveys (Carisi et al., 2016; Shustikova et al., 2019). Both sets of data are affected by large uncertainties. The accuracy of watermarks can be estimated to be around 0.5 m

(Dottori et al., 2013), while information on flood arrival times was obtained from newspaper reports, hence the location is uncertain and errors can be estimated to be up to 0.5-1 h. In spite of this, these data can be useful to compare the overall performance of the two hydraulic models and their sensitivity to spatial resolution and roughness.

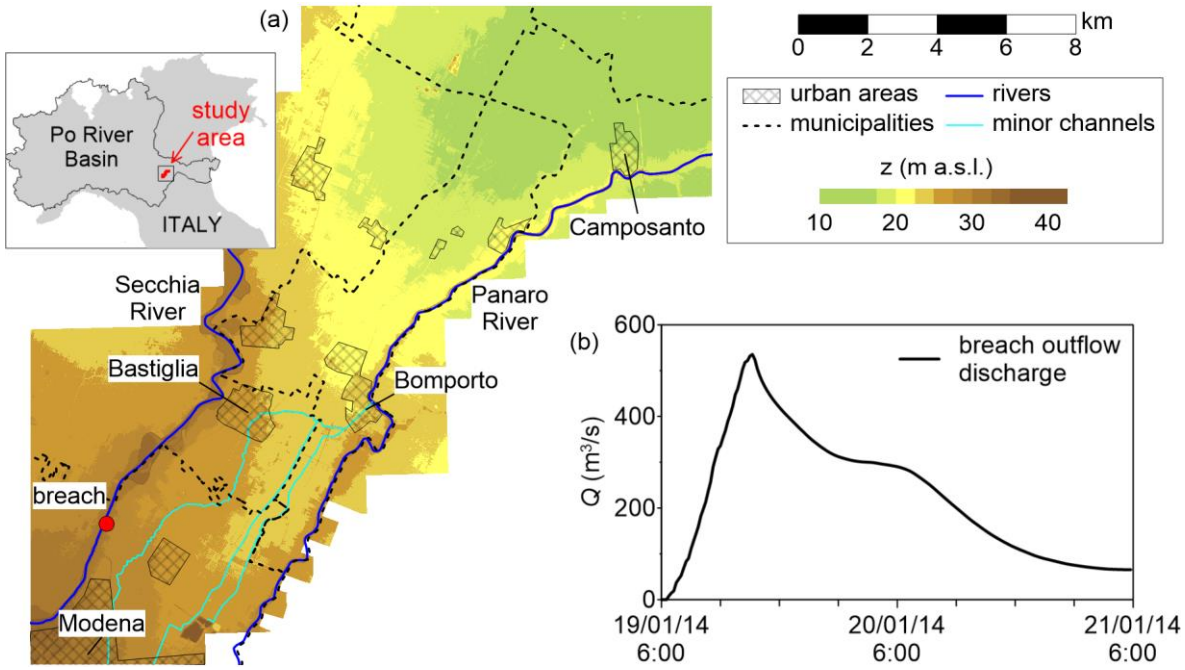

Figure 2 – (a) Study area for the Secchia test case: DTM of the area and terrain features; (b) discharge hydrograph flowing out of the breach, imposed as boundary condition.

4. Results

4.1 Po River

Table 2 reports the range of calibrated values for Manning's coefficient for the two models, and the corresponding RMSE of simulated and observed high watermarks in 171 locations. LISFLOOD-FP requires higher roughness values to obtain a correct prediction of the maximum water surface elevations, compared to PARFLOOD, in particular as regards the floodplains. In general, both models are able to reproduce the observed water elevation with a RMSE well below the observation error. The errors of individual points along the river (Figure 3) are in general below 50 cm, except for isolated cases in a few locations, and the mean error is equal to +0.03 m for PARFLOOD and to -0.04 m for LISFLOOD-FP. In general, there are regions in the domain where PARFLOOD overestimates and LISFLOOD-FP underestimates the maximum levels (e.g. 0-30 km), and other regions where the opposite is true (e.g. 180-220 km). The only significant trend towards over-prediction for both models can be observed in the downstream part of the domain, near

Pontelagoscuro. This narrow section (roughly 200 m wide) represents a “bottleneck”, which is not described well at this spatial resolution (30 m) due to the fictitious enlargement of embankments (Wing et al., 2019b). The problem could have been mitigated by manually modifying the mesh in this stretch (i.e. slightly shifting the levee locations to restore the correct floodway), or, even better, by increasing the spatial resolution locally. This possibility was not explored here because only PARFLOOD supports non-uniform grids.

Table 2 – Po River model calibration (30 m resolution): Manning’s coefficients and RMSE of simulated and observed high watermarks.

Model	Roughness coefficients ($m^{1/3}s$)		RMSE (m)
	Channel	Floodplain	
LISFLOOD-FP	0.032-0.043	0.095	0.34
PARFLOOD	0.025-0.045	0.050	0.26

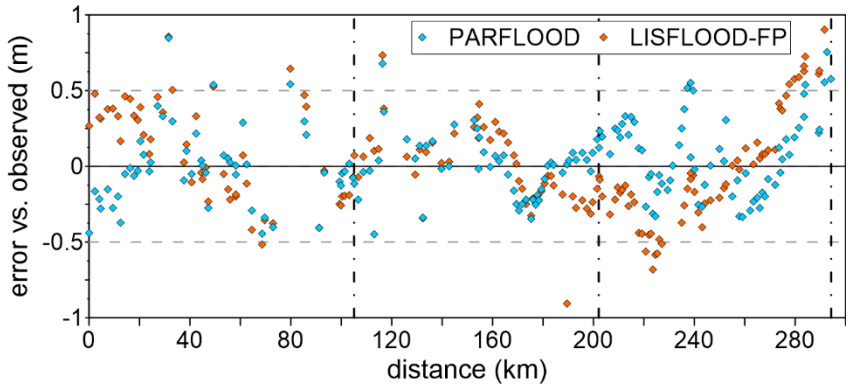

Figure 3 – Absolute errors of simulated maximum water surface elevations (30 m resolution) versus observations along the river. Vertical dashed lines indicate the position of Cremona, Borgoforte and Pontelagoscuro gauging stations.

Figure 4 compares the numerical results with the observed time series of water levels and discharges at three available river gauges (see Figure 1 for their position). Both models predict the water level hydrographs in the upstream gauges of Cremona and Borgoforte with acceptable accuracy (Figure 4a-b). Some discrepancies can be observed in the rising/falling limbs for both models, which can be ascribed to multiple reasons: (i) there are uncertainties in the upstream inflow, especially in the falling limb, due to the conversion of recorded levels into discharges using a single-valued rating curve instead of a looped one; (ii) during the event, overtopped minor embankments might have experienced breaching, which could lead to a more rapid filling of the floodplain behind, and this behavior was not considered in the simulations. Despite this, the maximum level is well caught (within ±25 cm compared to observations), and the timing of the peak is captured satisfactorily, being only slightly anticipated in Cremona (-12 h for LISFLOOD-FP; -4 h for PARFLOOD), and slightly delayed in Borgoforte (+5 h for LISFLOOD-FP; +1 h for PARFLOOD). Please notice that the peaks

of these hydrographs are quite “flat”, hence an uncertainty of a few hours is totally admissible. Downstream, at Pontelagoscuro gauging station (Figure 4c), both models largely overestimate the maximum level (+1.34 m for LISFLOOD-FP; +0.78 m for PARFLOOD). The peak is also delayed for PARFLOOD (+9 h), while timing is acceptable for LISFLOOD-FP (+5 h). As previously explained, this location is a “bottleneck”, where the mesh resolution (30 m) does not provide a good representation of the area available to flow.

Discharge time series at the same locations can be analyzed in Figure 4d-f. To ensure a fair comparison between simulations and observations, the figure also reports an uncertainty band that takes account of a 10% expected error associated to river discharges (Castellarin et al., 2011). At Cremona (Figure 4d), both numerical discharge time series lie within this band around the peak, although PARFLOOD slightly overestimates the maximum discharge (+4%). At Borgoforte (Figure 4e), both models predict a lower peak discharge compared to observations (-8% for LISFLOOD-FP, -4% for PARFLOOD). Finally, at Pontelagoscuro (Figure 4f), despite the discussed limitations of the model at this site, the peak discharge is captured satisfactorily with a tendency to overestimation for both models (+9% for LISFLOOD-FP, +10% for PARFLOOD). Overall, both models replicate the attenuation of the peak discharge along the river (Figures 4d-f).

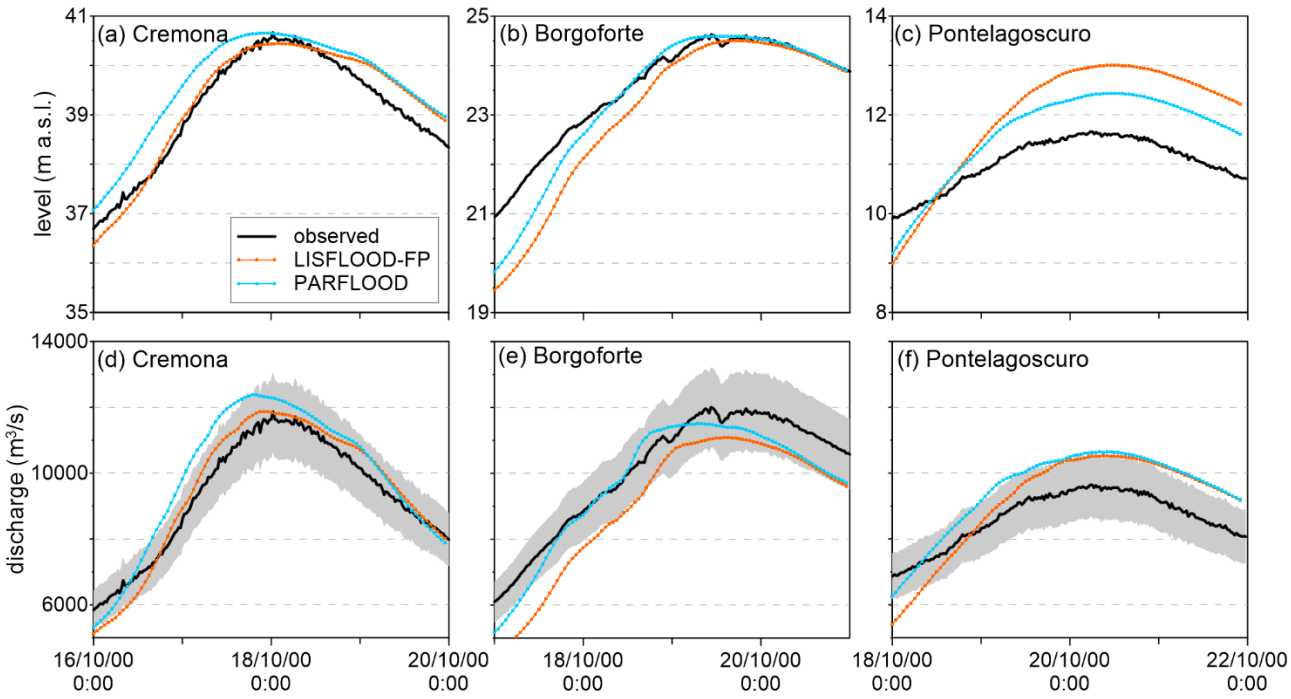

Figure 4 – Level (a-c) and discharge (d-f) time series in Cremona, Borgoforte, and Pontelagoscuro: comparison between measured values and simulations (30 m resolution) with PARFLOOD and LISFLOOD-FP. The grey band indicates an estimated 10% uncertainty on discharge observations. The time axis is reduced to improve readability.

Figure 5 depicts the maps of maximum water depths obtained from the simulations, which confirm that no overflows can be detected from the main embankments, and that most dyke-protected floodplains are inundated during the event and contribute to attenuating the peak flow downstream. In general, the differences between the two models are below 50 cm in the main channel (Figure 5c), and no systematic bias can be identified (see also Figure 3). In the mid-lower portion of the domain (around Borgoforte and downstream), slightly different filling levels are predicted inside the leveed floodplains as a consequence of slightly different in-channel depths, but this behavior is mainly related to the severity of the event and to the uncertainty in model calibration, rather than to the models' characteristics.

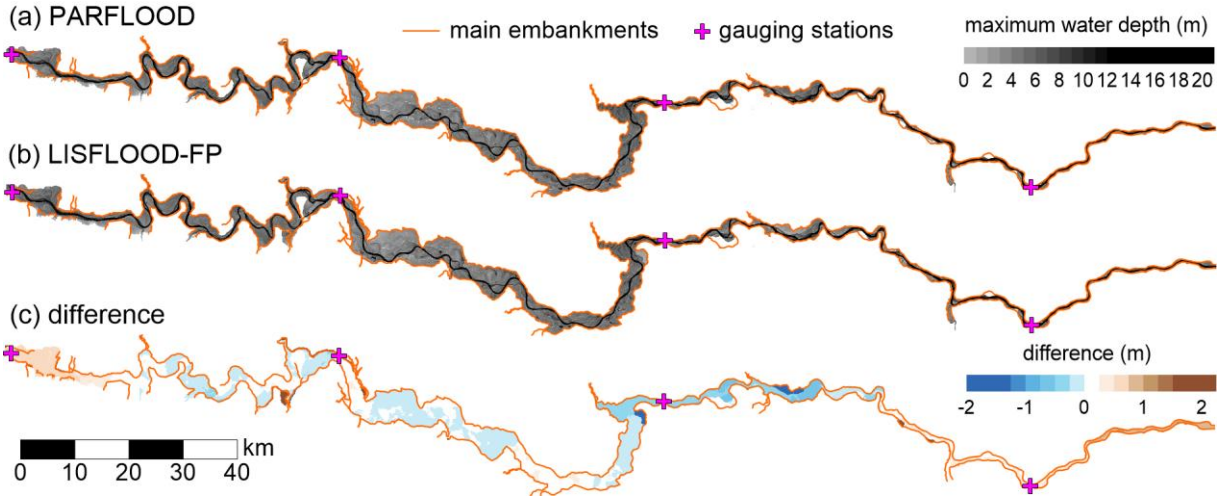

Figure 5 – Contour maps of maximum water depth for the Po River case study (30 m resolution) predicted by (a) PARFLOOD, and (b) LISFLOOD-FP. Panel (c) shows the contour map of differences between LISFLOOD-FP and PARFLOOD.

Compared to 1D models, 2D simulations bring additional value to river flow analyses, thanks to the detailed prediction of velocity fields, which can be of use for the identification of critical spots (e.g. high velocities near levees susceptible to erosion and instability). However, velocity measurements are not available for this event (and in general for field case studies), hence only an inter-model comparison can be performed here. Figure 6 shows the maps of maximum velocities obtained from the simulations with 30 m resolution. While the mean value of velocity maps is similar for the two models (0.75 m/s for PARFLOOD; 0.72 m/s for LISFLOOD-FP), the local distribution presents some differences, as shown in Figure 6c-d. The LISFLOOD-FP simulation provides higher velocity values than PARFLOOD along the river main channel, where the calibrated values of the roughness coefficient are similar for the two models (see Table 2). This difference is particularly noticeable (up to +1-2 m/s) at the outside bend of meanders, in locations where the largest velocities are obtained. Conversely, in floodplains, LISFLOOD-FP predicts lower velocities than PARFLOOD (difference below 0.6 m/s): in this areas, a smoother Manning's coefficient was assumed in PARFLOOD

simulations. The possible reason for these differences is further analyzed in Section 4.3. Finally, both models simulate very low velocities inside dyke-protected floodplains. However, on the landside slope of overtopped minor levees (see an example in Figure 7 for two floodplains upstream of Borgoforte), PARFLOOD predicts high maximum velocities (up to 3-3.5 m/s) and supercritical flow (the Froude number exceeds 1 in these spots, see Figure 7c). As the occurrence of transitions from subcritical to supercritical flow is localized and limited in time, LISFLOOD-FP provides stable results for this test case, despite the local-inertial approximation (Neal et al., 2012b).

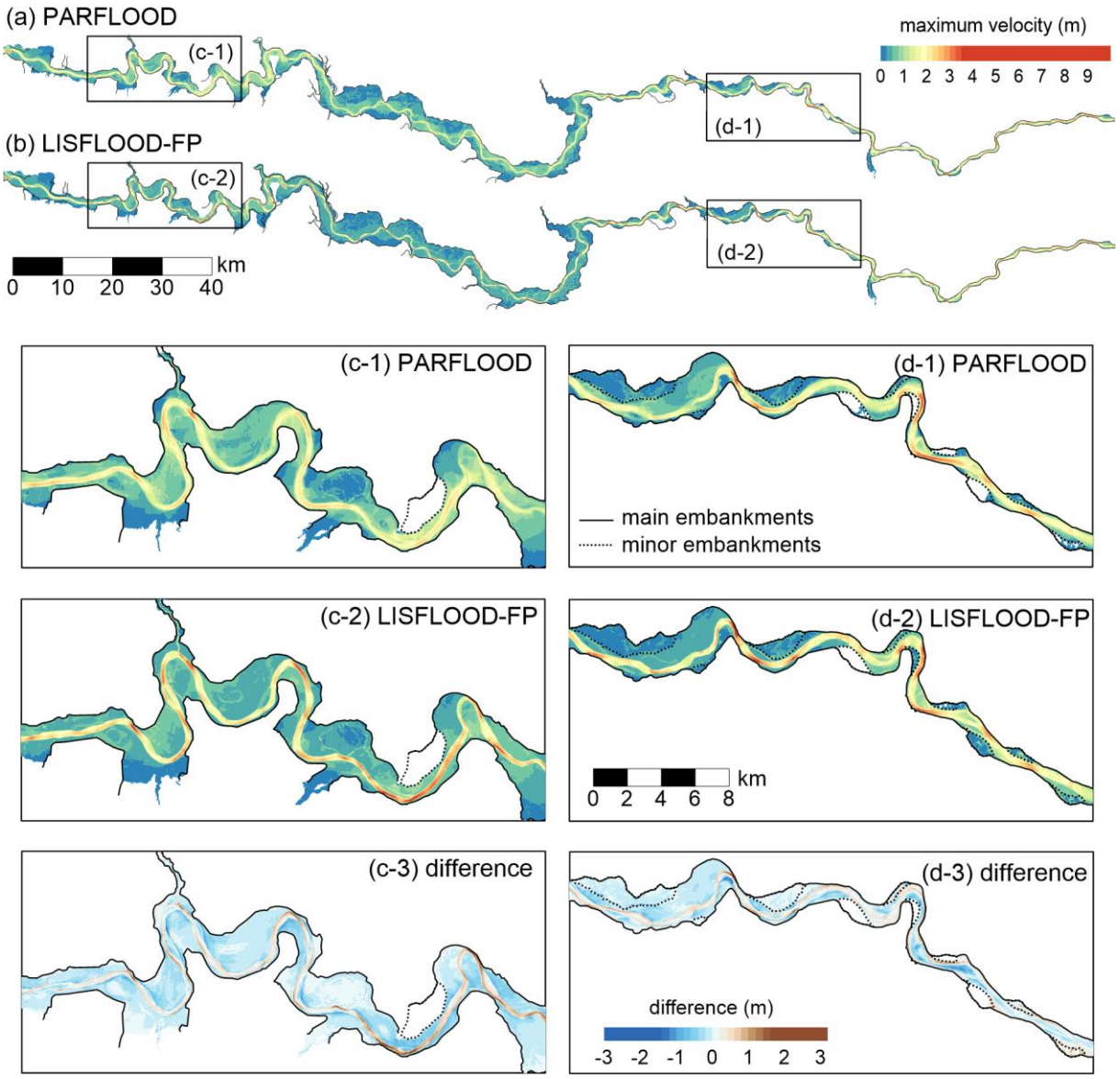

Figure 6 – Contour maps of maximum velocity for the Po River case study (30 m resolution) predicted by (a) PARFLOOD, and (b) LISFLOOD-FP. Panels (c)-(d) highlight the differences between LISFLOOD-FP and PARFLOOD results at selected locations.

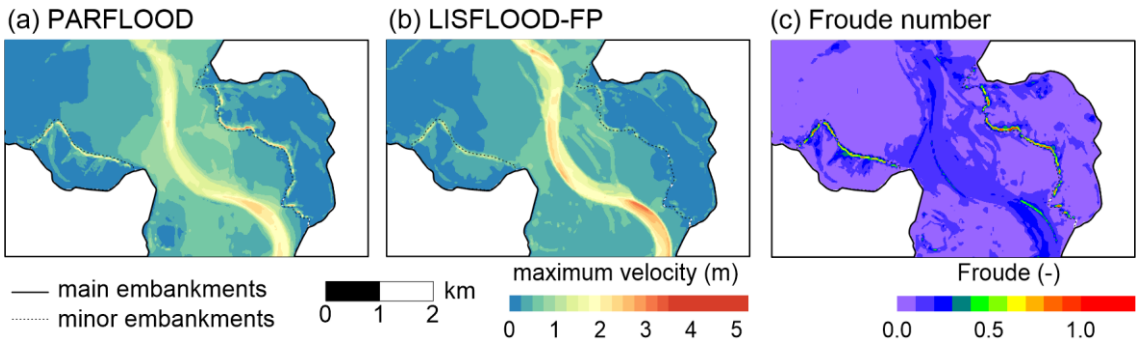

Figure 7 – Detail of the maximum velocity near two dyke-protected floodplains (upstream of Borgoforte), as predicted by (a) PARFLOOD, and (b) LISFLOOD-FP (30 m resolution); (c) Froude number predicted by PARFLOOD.

Simulations performed with coarser mesh resolutions lead to less satisfactory results. The maximum water surface elevations are overestimated compared to the observations for both models: the RMSE is equal to 0.68 m for PARFLOOD, and to 0.39 m for LISFLOOD-FP when using the 50 m-resolution mesh. This suggests that the set of roughness coefficients previously calibrated for LISFLOOD-FP is still adequate to simulate the event even when the resolution is coarsened from 30 m to 50 m, while for this case study PARFLOOD requires mesh-dependent coefficients. The largest deviations from high water marks are found downstream, near Pontelagoscuro: here, the peak level is significantly overestimated (+1.53 m for LISFLOOD-FP; +1.74 m for PARFLOOD). For both models, errors on the peak discharges at Cremona, Borgoforte and Pontelagoscuro remain within the 10% uncertainty band, and the maximum velocities are similar to the configuration with 30 m (differences in the order of ±0.5 m/s). However, overflows are observed in some upstream locations for both models. As regards the simulations performed with the 100 m-resolution mesh, the capacity of the floodplain between the main embankments is reduced to the extent that the water spilled out from the floodplains in multiple locations. For both resolutions, the problem lies in the misrepresentation of embankments: previous studies (Shustikova et al., 2019; Wing et al., 2019b) suggest that coarse models often misestimate flood parameters due to the difficulty of representing linear features finer than the mesh resolution. Overall, the 100 m-configuration is considered not fit for this case study and should be disqualified, while the adherence to observations for the 50 m configuration is still adequate (except near Pontelagoscuro) as regards LISFLOOD-FP, and can probably be improved by calibrating a specific set of roughness coefficients for this spatial resolution as regards PARFLOOD. This additional parameter tuning was not performed in this study, since the aim of low-resolution simulations was mainly to compare the models' runtimes when coarser grids were adopted (see Section 4.4).

4.2 Secchia River

Overall, 9 simulations were performed with each model (3 grids × 3 roughness values). In the following, we will refer to each test configuration with a label including both the grid size (5, 25, 50 m) and the type of roughness for the rural areas ("S" = smooth value, i.e. 0.03 $m^{-1/3}s$; "C" = central value, i.e. 0.05 $m^{-1/3}s$; "R" = rough value, i.e. 0.07 $m^{-1/3}s$). For example, the simulations performed with the 25 m resolution grid and Manning's coefficient equal to 0.05 $m^{-1/3}s$ will be labelled "25_C". Test configurations are summarized in Table 3.

Table 3 – Main characteristics of the 9 simulations performed with each model, and main results: F parameter, and RMSE of water depth at known points. Note that simulation 5_C with PARFLOOD is used as reference, for both models, for computing F (Eq. 11).

Test	**Grid size (m)**	***n*** **($m^{-1/3}s$) rural**	***F*** **(%)**		**RMSE (m)**	
			PARFLOOD	**LISFLOOD-FP**	**PARFLOOD**	**LISFLOOD-FP**
5_S	5	0.03	93	84	0.35	0.37
5_C	5	0.05	-	91	0.35	0.35
5_R	5	0.07	94	97	0.35	0.34
25_S	25	0.03	82	81	0.37	0.34
25_C	25	0.05	84	81	0.37	0.33
25_R	25	0.07	84	82	0.37	0.33
50_S	50	0.03	79	78	0.42	0.40
50_C	50	0.05	79	78	0.41	0.39
50_R	50	0.07	79	78	0.41	0.39

The capability of the PARFLOOD model of reproducing the flood evolution and inundation extent for this event was assessed in a previous study (Vacondio et al., 2016), where the 5 m mesh and the calibrated value of 0.05 $m^{1/3}s$ for the roughness coefficient in rural areas were adopted. For this reason, the flooded area obtained from the simulation performed with these parameters (labelled "5_C") is here assumed as reference (i.e. "observed") for comparing the model performances of both models (i.e., LISFLOOD-FP and PARFLOOD) in terms of inundation extent, by evaluating the parameter *F* (e.g. Bates & De Roo, 2000), defined as follows:

$$F = \frac{A_{sim} \cap A_{ref}}{A_{sim} \cup A_{ref}}\% \tag{11}$$

where A_{sim} and A_{ref} represent the simulated and reference flooded areas, respectively.

Figure 8 compares the maps of maximum water depths predicted by the two models for configuration "5_C". The inundation extent is very similar, also thanks to the partial confinement guaranteed by the Panaro River levee and by other minor embankments; only marginal differences can be

observed, especially downstream (North). Overall, the predicted flooded area is equal to 49.2 km^2 according to PARFLOOD, and 50.3 km^2 according to LISFLOOD-FP. The latter simulation gives a parameter *F* equal to 91% (see Table 3), which implies a very good correspondence with the reference PARFLOOD simulation.

The differences between predicted and observed water levels at 46 watermarks are also reported in Figure 8. The RMSE (see Table 3) is equal to 0.35 m for both models and indicates an acceptable agreement with observations. LISFLOOD-FP performs slightly better in the focus area of Bastiglia: the RMSE for the subset of 25 points surveyed in this area is equal to 0.26 m (vs. 0.31 m for PARFLOOD), while the mean difference is +0.16 m for LISFLOOD-FP, and +0.22 m for PARFLOOD. No significant trend of under/overestimation can be detected. On the other hand, in Bomporto (the other focus area), both models overestimate the observed water depths; the mean difference between simulated and observed levels (limited to the 11 points surveyed here) is +0.40 m for PARFLOOD, and +0.46 m for LISFLOOD-FP. In this area, PARFLOOD is slightly more adherent to observations than LISFLOOD-FP, since the local RMSE is 0.45 m (vs. 0.51 m for LISFLOOD-FP). It is worth noting that, during the event, water accumulated in Bomporto and formed a “lake at rest” due to the local topography (bounded by the levees of the Panaro River and of the Naviglio Channel); hence, deviations from observations in this area can also be partly attributable to the uncertainties in the breach outflow discharge, which may lead to a slight overestimation of the flooded volume.

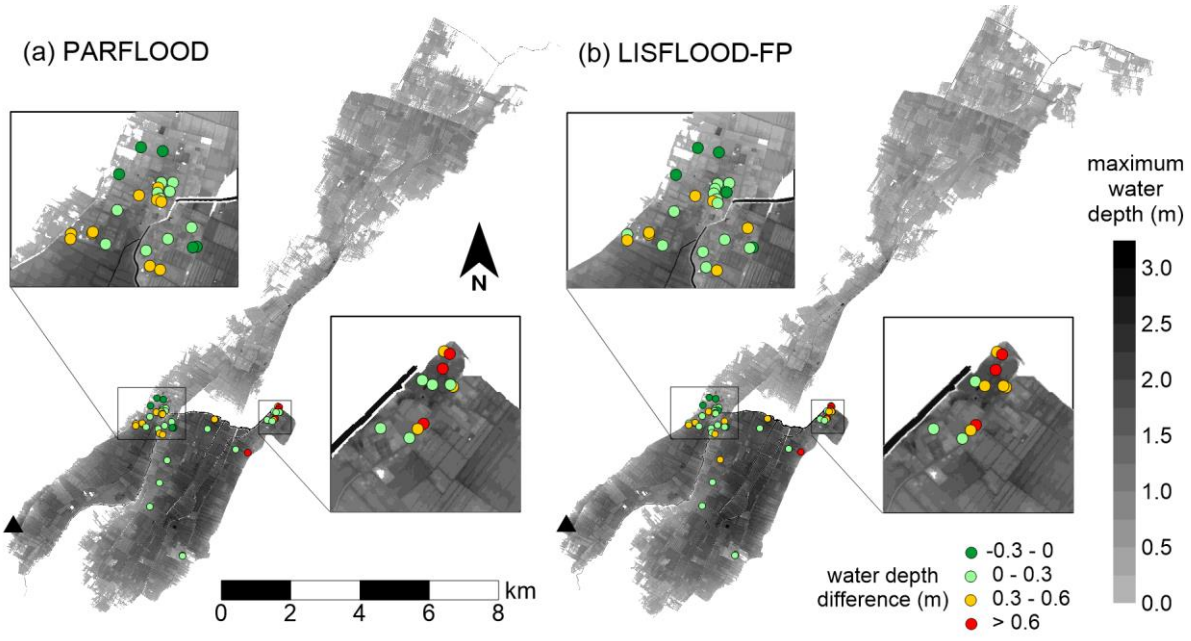

Figure 8 – Contour maps of maximum water depth for configuration “5_C” predicted by (a) PARFLOOD, and (b) LISFLOOD-FP; difference between simulated and observed water depth at known points. The inserts are referred to the urban areas of Bastiglia (upper) and Bomporto (lower). The black triangle identifies the breach position (inflow).

Table 3 reports the values of the *F* parameter for all the 9 simulations (different grid size and roughness) performed with each model. At the highest resolution (5 m), the overall flooded area only slightly differs from the reference simulation, even when the roughness coefficient is varied. As regards the PARFLOOD simulations, the values of *F* are equal to 93-94% using either smoother or rougher values of Manning's coefficient. Conversely, for LISFLOOD-FP the best agreement is actually obtained from the simulation with the roughest coefficient 0.07 $m^{1/3}s$ (*F* = 97%), while the adoption of a smoother coefficient gives a less satisfactory value of 84%, due to the slight overestimation of the flooded area to the North (see Figure 9, which compares the inundation extents obtained from different simulations with the reference one).

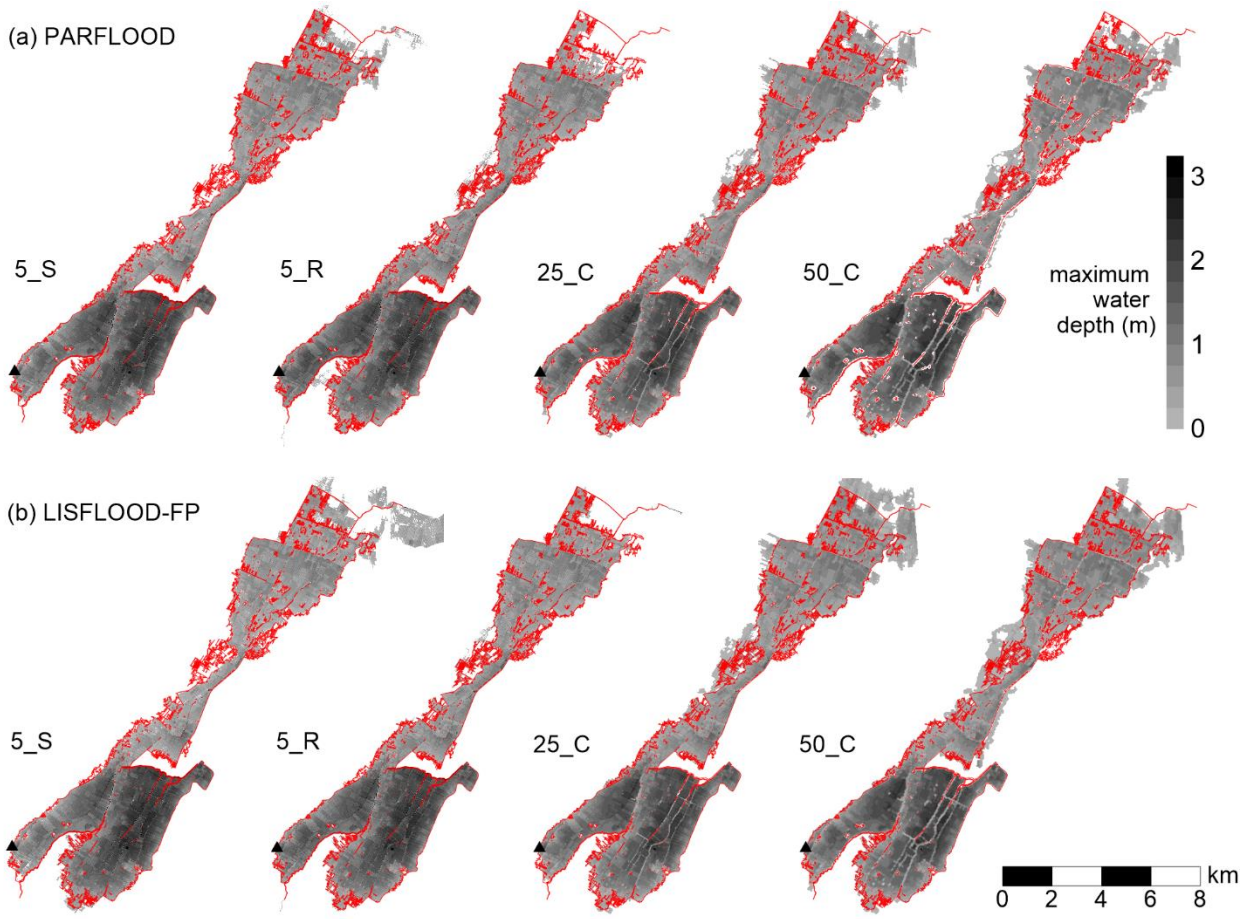

Figure 9 – Maximum water depth predicted by (a) PARFLOOD, and (b) LISFLOOD-FP, with different roughness (5_S and 5_R) and resolution (25_C and 50_C), compared with the reference flooded area (red line). The black triangle identifies the breach position (inflow).

When a lower grid resolution is adopted, both models slightly overestimate the flooded area (Figure 9). Simulations with the 25 m mesh give a value for the *F* parameter around 82-84% for PARFLOOD, and 81-82% for LISFLOOD-FP (only marginally variable with the roughness coefficient). Similarly, the *F* value computed for all simulations performed with the coarsest resolution (50 m) is equal to 79% for PARFLOOD and to 78% for LISFLOOD-FP, regardless of the assumptions on Manning's

coefficient. The overestimation of the inundation extent at coarse resolutions is often observed in real applications (Savage et al., 2016b), and is related to the poorer terrain description. Moreover, the inclusion of embankments, which are artificially widened at low resolution, may reduce the volume available for water storage (Wing et al., 2019b), similarly to the Po River case study. For example, let us consider the area bounded by the levees of the Panaro River and of the Naviglio Channel (the western channel in Figure 2), where water accumulates in a "lake-at-rest" fashion: when the observed maximum water surface elevation (approximately 26 m a.s.l.) is reached, the volume that can be stored in this area reduces by 9% and by 20% for the 25 m and 50 m meshes, respectively, compared to the 5 m mesh. This generates an increase in the amount of flood volume that flows downstream, and consequently in the flooded area downstream. However, neglecting the presence of minor embankments would lead to a much less accurate prediction of the flooding dynamics and inundation extent (see the results by Shustikova et al., 2019).

The agreement with the high watermarks was also analyzed for all simulations (see values of RMSE in Table 3). While the PARFLOOD model provides the same RMSE for all the high-resolution simulations (0.35 m), slight differences can be observed for the LISFLOOD-FP simulations. Among these, the best performance is obtained with the roughest coefficient (0.34 m). When a coarser resolution is used, the values of RMSE are not particularly sensitive to roughness for both models. However, compared to the results of simulations with higher resolution, PARFLOOD gives a slightly higher RMSE (0.37 m for the 25 m mesh, and 0.41-0.42 m for the 50 m mesh). Instead, LISFLOOD-FP performs similarly (RMSE equal to 0.33-0.34 m) when the 25 m mesh is used, while the RMSE increases to 0.39-0.40 m with the 50 m mesh. In all cases, the RMSEs for both models are within the data observation error (<0.5 m).

The maps of flood arrival times were also obtained from all simulations, even if Figure 10 reports only 5 test configurations for each model. Moreover, the extent of the flooded area at 12, 24, 36, and 48 h is plotted in Figure 10c-d for these tests. As expected, the roughness coefficient adopted to describe the rural areas remarkably affects the flood propagation, and the flooded area at a fixed time increases when Manning's coefficient is reduced (i.e. the inundation propagates faster). This is true for both models. However, as regards the high-resolution mesh, simulations performed with LISFLOOD-FP are slightly more influenced by roughness compared to those performed with PARFLOOD, especially upstream of Bomporto. Comparable maps of flood arrival times are obtained from simulation "5_C" with PARFLOOD and "5_R" with LISFLOOD-FP. This means that the flood arrival time at a given point is larger for PARFLOOD than for LISFLOOD-FP, when the same roughness coefficient is adopted. Faster arrival times in a LISFLOOD-FP simulation (with the local-inertial approximation) than in a fully SWE simulation are also reported by Neal et al. (2012b) for a dam-break case. This fact was related to the adoption of decoupled equations in the *x*- and *y*-direction (which leads to the creation of preferential flow pathways along the diagonal, as discussed by Neal et al., 2012b, and more recently by Cozzolino et al., 2021), to numerical diffusion, and, to a

lesser extent, to the wetting and drying treatment. When the resolution is coarsened, both models provide arrival times that are quite similar to those obtained with the high-resolution mesh up to 12 h, whereas larger differences can be observed between the results of high- and low-resolution simulations in the 24-48 h time interval. Finally, simulations performed with the 25 m and 50 m meshes (adopting the same model and same roughness coefficient) provide comparable maps of flood arrival times for both LISFLOOD-FP and PARFLOOD.

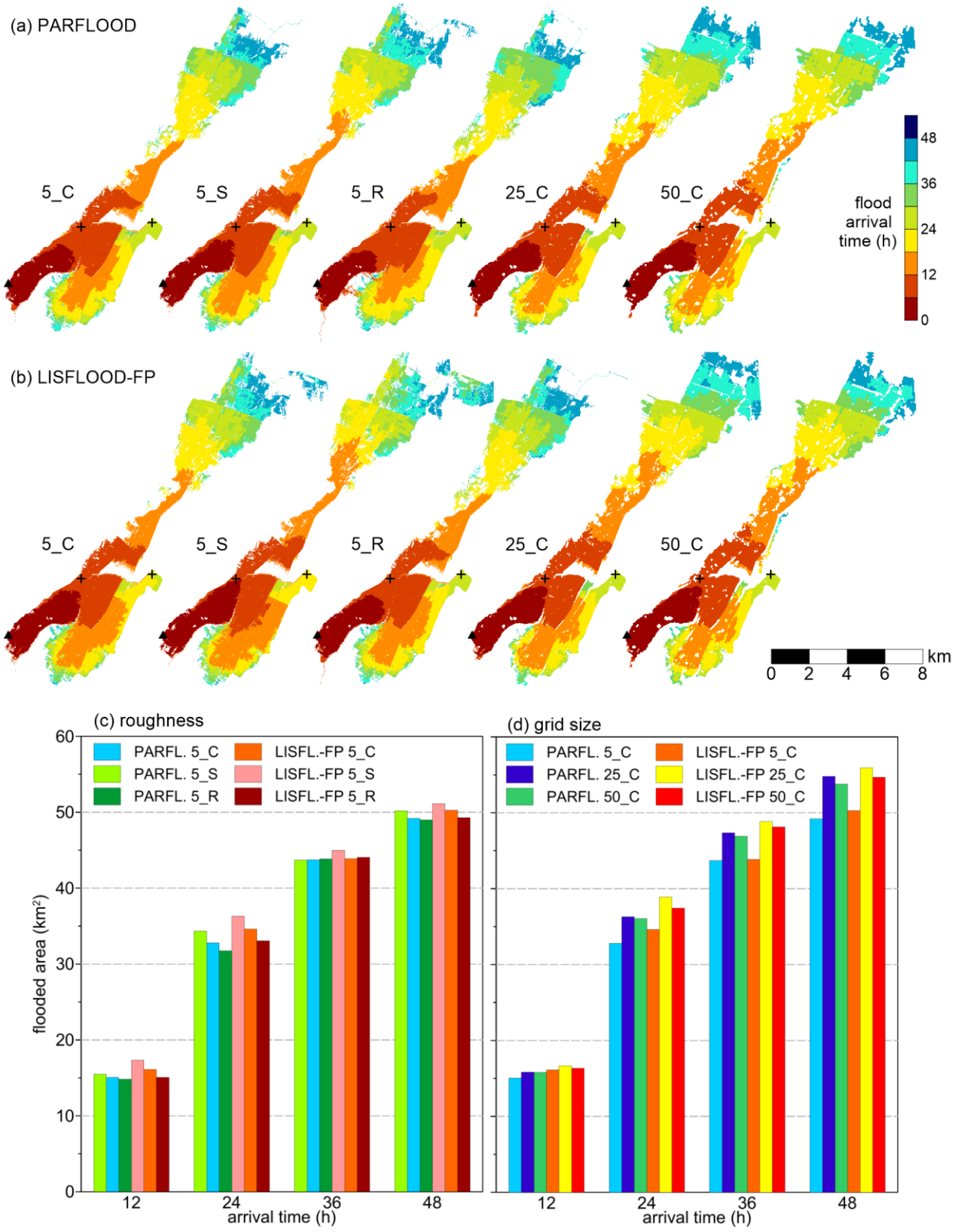

Figure 10 – Flood arrival times predicted by (a) PARFLOOD, and (b) LISFLOOD-FP, with different roughness (5_S and 5_R) and resolution (25_C and 50_C), compared with the reference configuration (5_C). The crosses identify the two locations of the observed arrival times, while the black triangle indicates the breach position (inflow). Panels (c)-(d) compare the flooded area at selected times for different roughness (c), and for different grid size (d).

Besides the comparison between the two models and between different configurations, simulated arrival times can also be compared with the observed arrival times at two locations (the urban areas of Bastiglia and Bomporto; see locations in Figure 10a-b). The difference between simulated and observed arrival time for each model and test configuration is represented in Figure 11. Please notice that, given the large uncertainty in the observed values (up to 0.5-1 h), simulated values were rounded to quarters for the comparison. Regardless of the resolution, PARFLOOD predicts the flood arrival in Bastiglia quite well using the central value of the roughness coefficient (0.05 $m^{1/3}s$), although the error is acceptable (below 1 h) for all configurations. Conversely, LISFLOOD-FP provides better results in Bastiglia with the roughest value (0.07 $m^{1/3}s$); in this case, the flood arrival time is anticipated up to 1.5 hours when the smoothest value of Manning's coefficient is adopted. The inundation of Bastiglia occurred only 7 h after the breach opening, without any significant obstacle to slow down the flooding. In Bomporto, instead, the inundation arrived after approximately 27 h from the breach opening, thanks to the obstruction to flood propagation provided by the levees of minor channels, which were eventually circumvented by water. This complexity in the flood dynamics affects the numerical results, as shown by their higher sensitivity to roughness and grid size as regards the arrival times in Bomporto (Figure 11b). At high resolution, LISFLOOD-FP anticipates the flood arrival time for all roughness coefficients, and the best performance is obtained for the roughest value 0.07 $m^{1/3}s$ (though the error is -1.5 h). Conversely, PARFLOOD correctly predicts the inundation of Bomporto using the central value 0.05 $m^{1/3}s$, while errors are up to 1.5 h if different values are used. At lower resolutions, LISFLOOD-FP predicts the correct arrival time using the central value, while PARFLOOD exhibits a slightly larger error (up to 1.25 h). However, the range of flood arrival times using different roughness coefficients is much larger for LISFLOOD-FP (about 5 h) than for PARFLOOD (about 3-3.5 h). Results in Bomporto, especially for LISFLOOD-FP, are somehow in contrast with the general expectation that the use of fine resolution grids produces later arrival times compared to coarser grids as a result of a more accurate terrain description. However, in this case study, the incorporation of the main embankments in the mesh guarantees the correct representation of the topography and of the inundation dynamics for all grid sizes, so this tendency may not be detected.

Overall, with equal roughness coefficient, PARFLOOD provides similar arrival times throughout different resolutions, while LISFLOOD-FP is slightly more sensitive to grid size switching from high to low resolution; however, simulations performed with coarse meshes (25 m and 50 m) produce almost identical flood arrival times. As regards the sensitivity to the values of the roughness coefficient for rural areas, similar trends are observed in Bastiglia (range of about 1.5 h regardless of the grid size) for both models, whereas simulated arrival times in Bomporto are more influenced by this parameter for all resolutions, especially for LISFLOOD-FP.

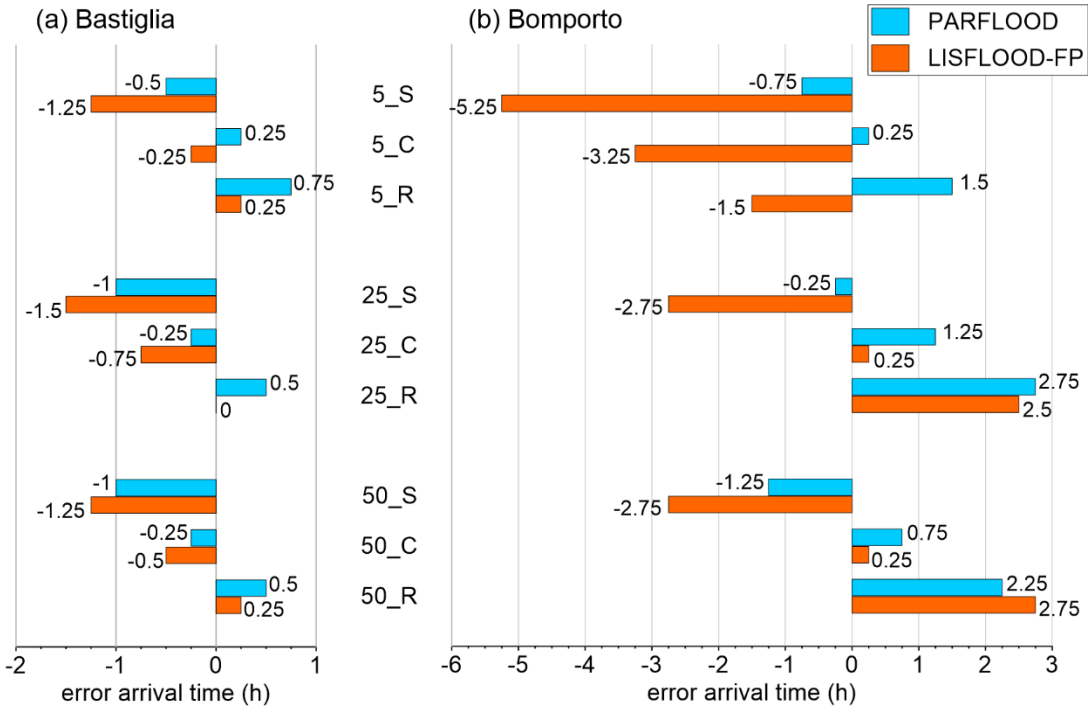

Figure 11 – Difference between simulated and observed flood arrival times at (a) Bastiglia, and (b) Bomporto, predicted by the two models for all test configurations.

Results presented so far suggest that the configurations that best fit the observations are 5_C for PARFLOOD and 5_R for LISFLOOD-FP. However, the value of Manning's coefficient that guarantees the best prediction for PARFLOOD is the same (0.05 $m^{-1/3}s$) for all resolutions, while LISFLOOD-FP switches from the roughest one (0.07 $m^{-1/3}s$) for the high-resolution mesh to the "central" one for the coarser grids.

In flood hazard mapping, another important variable to be considered is the flow velocity, which has consequences on the safety of pedestrians and vehicles (e.g. Arrighi et al., 2019), and is an important component of flood damage models (Merz et al., 2013). Only an inter-model comparison is performed here, since velocity measurements are obviously unavailable for this event. The maps of maximum flow velocities for selected configurations are reported in Figure 12. Overall, velocity values remain well below 1 m/s in most of the domain, except for local spots where values up to 1.5-2 m/s are obtained, especially in simulations with low roughness. Moreover, both models predict high velocities (up to 3-7 m/s, depending on the model and configuration) at the breach location: here, inter-model differences can also be ascribed to the implementation of boundary conditions in the two codes. Please notice that the color ramp in Figure 12 is saturated at 1.5 m/s in order to ease the visual comparison of maps.

The inter-model comparison of these maps somehow confirms the trend that could be anticipated from the analysis of flood arrival times, that is, other things being equal, LISFLOOD-FP predicts higher flow velocities than PARFLOOD. For example, in the base configuration (5_C), the mean value for the maximum velocity in the flooded cells is equal to 0.29 m/s for LISFLOOD-FP and to

0.19 m/s for PARFLOOD, while the median values are 0.23 and 0.15 m/s, respectively. The velocity value of 0.4 m/s is exceeded by only 10% of the flooded cells in the domain for PARFLOOD, against 25% for LISFLOOD-FP. Similar trends can be observed for other high-resolution simulations, although differences in median values are slightly larger for configuration 5_S (0.28 m/s for LISFLOOD-FP and 0.17 m/s for PARFLOOD) and slightly lower for configuration 5_R (0.2 m/s for LISFLOOD-FP and 0.13 m/s for PARFLOOD), as expected. If we compare the "best fit" simulations, LISFLOOD-FP (configuration 5_R) still predicts higher maximum velocities than PARFLOOD (configuration 5_C): the mean values are equal to 0.25 m/s for the former model, and to 0.19 m/s for the latter, while the velocity of 0.48 m/s is exceeded only by 5% of PARFLOOD flooded cells (vs. 10% for LISFLOOD-FP).

At low resolutions (25_C and 50_C), maximum velocities are slightly lower than those of the high-resolution simulation (5_C) performed with the same model; for example, the mean and median values are 16% and 13% lower, respectively (for both models). However, local high values of maximum velocity are remarkably reduced, especially for LISFLOOD-FP. When the same model is used, simulations with 25 m and 50 m provide very similar overall results. At coarse resolution, LISFLOOD-FP still predicts slightly higher maximum velocities than PARFLOOD with equal roughness coefficient.

The difference between the maximum velocities predicted by the two models can be better observed in Figure 13, which zooms on the portion of the domain around Bastiglia. Inside the urban area (represented by means of a higher roughness coefficient than the one adopted for rural areas), velocities are slightly lower than outside, and this is particularly noticeable for LISFLOOD-FP results. An interesting observation is the fact that, at high resolution, the maximum velocity predicted by LISFLOOD-FP seems influenced by micro-topographic features in the terrain, such as small ditches and furrows, while PARFLOOD provides slightly more uniform results. When the roughness is increased, this effect can still be observed, even if the velocities are lower (see for example configuration 5_R). When the resolution is reduced (as for example for configuration 25_C), this behavior can no longer be clearly noticed. This particular velocity pattern, which is only evident in LISFLOOD-FP results, can partly be ascribed to the different way in which velocity is computed for the two models (see Section 2.3), but another possible reason is analyzed in Section 4.3.

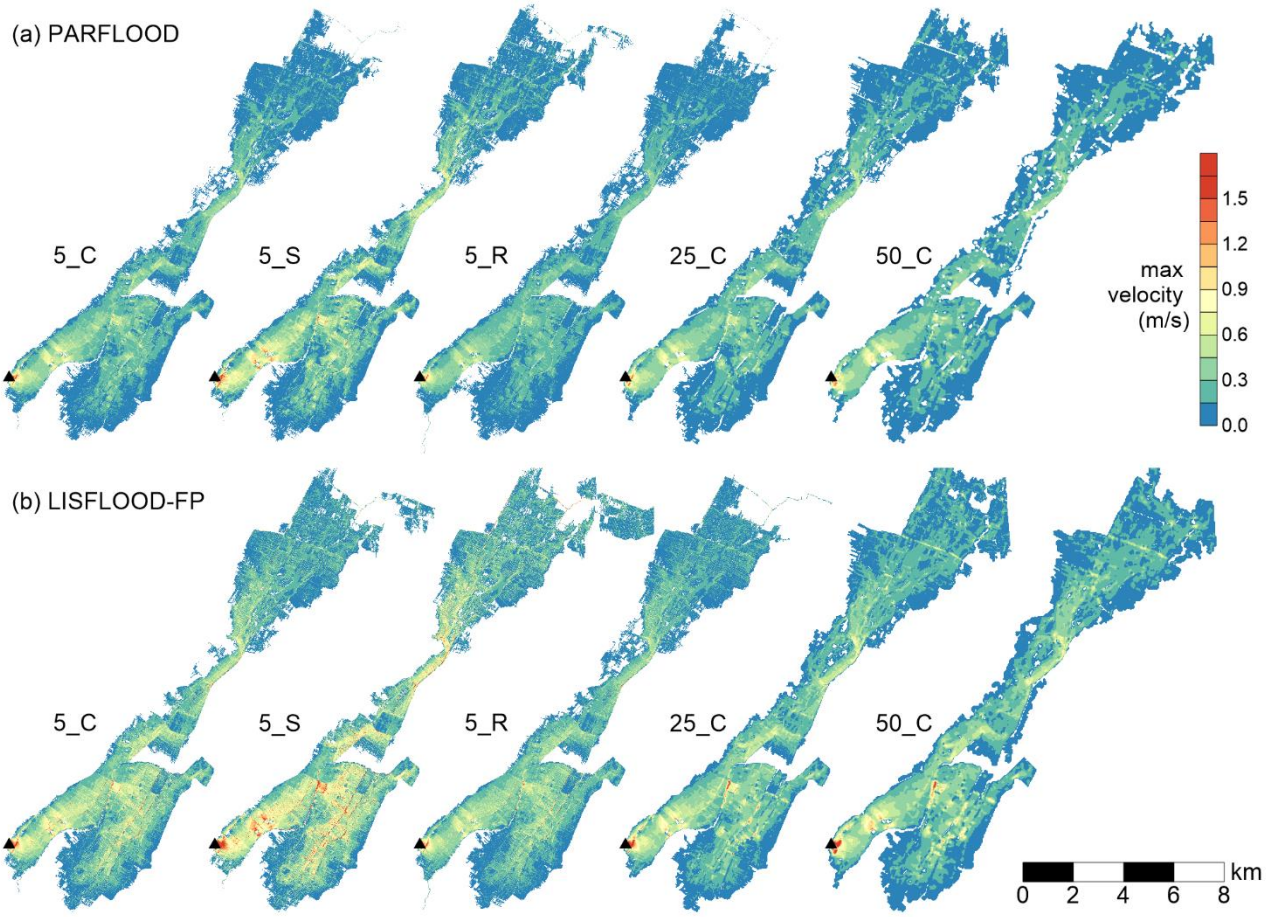

Figure 12 – Maps of maximum flow velocity (magnitude) by (a) PARFLOOD, and (b) LISFLOOD-FP, with different roughness (5_S and 5_R) and resolution (25_C and 50_C), compared with the reference configuration (5_C). The black triangle indicates the breach position (inflow).

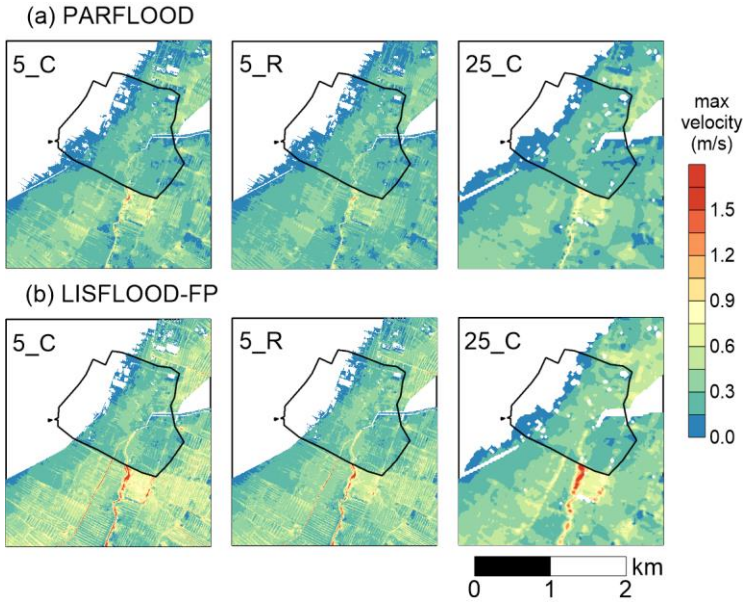

Figure 13 – Detail of maximum flow velocity (magnitude) predicted by (a) PARFLOOD, and (b) LISFLOOD-FP, in the focus area of Bastiglia (identified with a black line) for configurations 5_C, 5_R, and 25_C.

4.3 Convective acceleration analysis

We performed an additional analysis concerning the relative importance of the different terms of the SWEs for the two previous case studies. For this purpose, the momentum equations were re-written in 2D non-conservative form as follows:

$$\begin{cases} \underbrace{\frac{1}{g}\frac{\partial u}{\partial t}}_{\text{(i)}} + \underbrace{\left[\frac{u}{g}\frac{\partial u}{\partial x} + \frac{v}{g}\frac{\partial u}{\partial y}\right]}_{\text{(ii)}} + \underbrace{\frac{\partial \eta}{\partial x}}_{\text{(iii)}} + \underbrace{S_{fx}}_{\text{(iv)}} = 0 \\ \underbrace{\frac{1}{g}\frac{\partial v}{\partial t}}_{\text{(i)}} + \underbrace{\left[\frac{v}{g}\frac{\partial u}{\partial x} + \frac{u}{g}\frac{\partial v}{\partial x} + \frac{v}{g}\frac{\partial v}{\partial y}\right]}_{\text{(ii)}} + \underbrace{\frac{\partial \eta}{\partial y}}_{\text{(iii)}} + \underbrace{S_{fy}}_{\text{(iv)}} = 0 \end{cases} \quad (12)$$

In this non-dimensional form, each term represents a slope (Cunge et al., 1980), i.e. (i) local acceleration; (ii) convective acceleration; (iii) free-surface slope; and (iv) friction slope. The first two terms are the “inertial terms” or “acceleration slopes”. Please note that the second term is neglected in the LISFLOOD-FP approximation. Numerical results provided by PARFLOOD (which solves the fully dynamic SWEs) were elaborated to compute the derivatives and, consequently, the absolute values of the four terms in Eq. 12.

Figure 14 represents the order of magnitude of all terms (both *x* and *y* directions) along the Po River reach near Borgoforte gauging station, approximately at the time of the peak. The local acceleration is negligible compared to the other terms (below 10^{-6}-10^{-5} almost everywhere, see Figure 14a-d). The free-surface slope (Figure 14c-f) is certainly the most significant term in the whole reach, followed by the friction slope (Figure 14g-h): this means that the local-inertial (or even diffusive) approximation can be considered suitable for modelling this event. However, Figure 14b-e shows that, even at the relatively large resolution (30 m) adopted, the convective acceleration term is not completely negligible along the main channel, especially downstream where the river width decreases, and the path is more winding. Here, the spatial variation of the velocity head is fostered by differences in flow direction, bed elevation and roughness. While the “global” effect induced by the convective acceleration term on flood propagation and maximum levels can be somehow compensated in the simplified model LISFLOOD-FP by adjusting the roughness coefficients, neglecting its importance probably leads to the observed differences in the velocity distribution in the main channel compared to a fully dynamic model (see Figure 6). On the other hand, this term does not influence the inundation of dyke-protected floodplains, dominated by the free-surface slope, which can be over 10^{-2} during the overtopping of minor embankments.

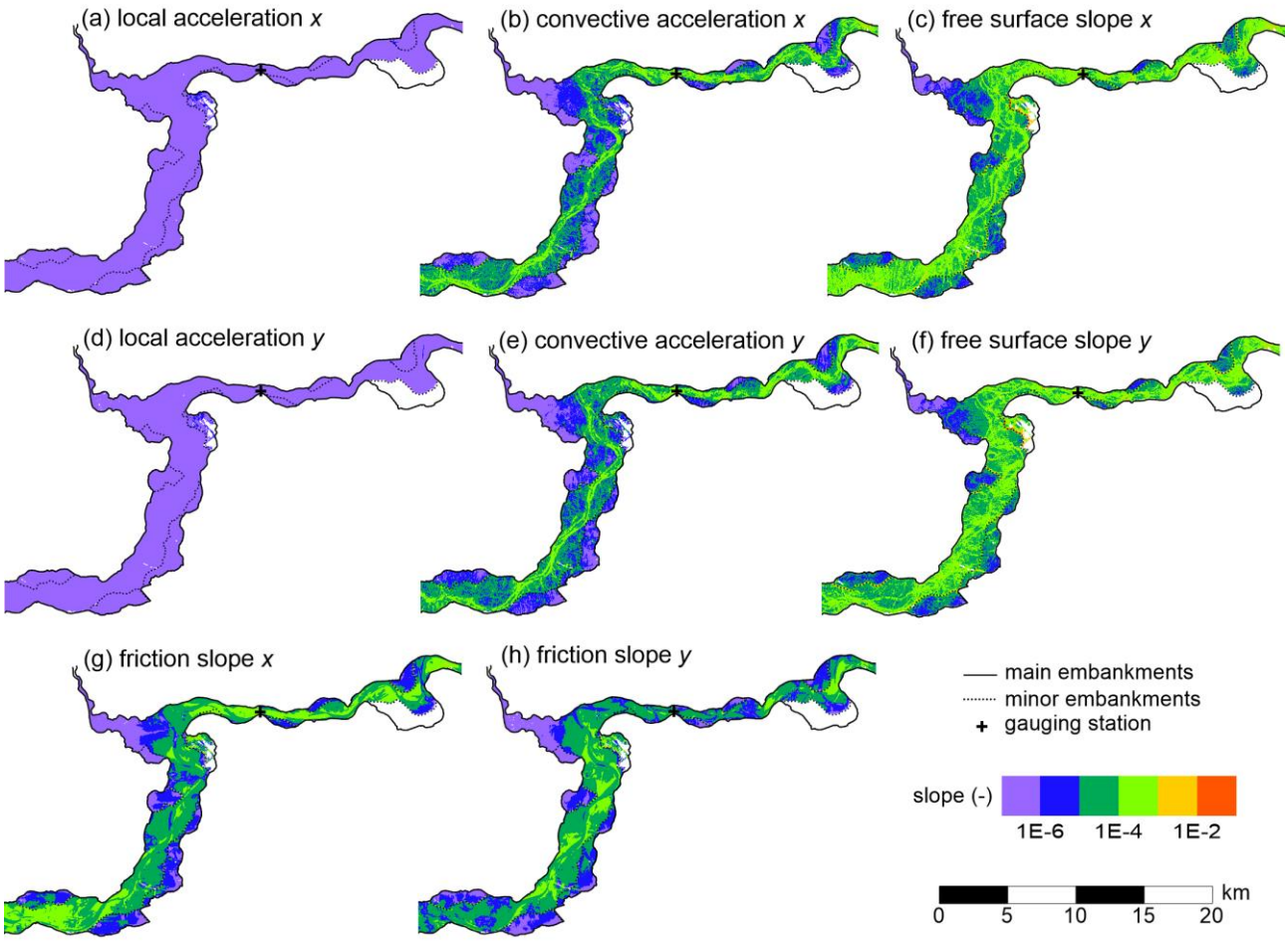

Figure 14 – Contour maps of the four slope terms of Eq. 12 along the x and y directions for the Po River case study (30 m resolution), predicted by PARFLOOD, near the gauging station of Borgoforte, close to the time of peak (00:00, 19 October 2000).

A similar analysis was repeated for the Secchia case study (configurations 5_C and 25_C). Figure 15 shows the maps of the convective acceleration, free-surface and friction slopes along the *x* and *y* directions, obtained from the PARFLOOD simulations, 8 hours after the breach opening (when flooding had just reached the urban area of Bastiglia). Note that local acceleration is negligible compared to the other terms and is not reported. At the highest resolution (Figure 15a), the free-surface and friction slopes terms dominate the phenomenon, while convective acceleration is approximately one order of magnitude lower, being relevant only in few cells characterized by large velocity variations due to micro-topography. When the mesh size increases (Figure 15b), term (ii) of Eq. 12 becomes negligible compared to terms (iii) and (iv) in the whole domain. This confirms the suitability of the local-inertial approximation when a coarse grid is adopted, while the effects of micro-topography at high resolution might require the use of fully dynamic equations for obtaining an accurate estimation of the velocity distribution. Indeed, the fact that LISFLOOD-FP neglects the convective acceleration probably determines the difference shown in Figure 13.

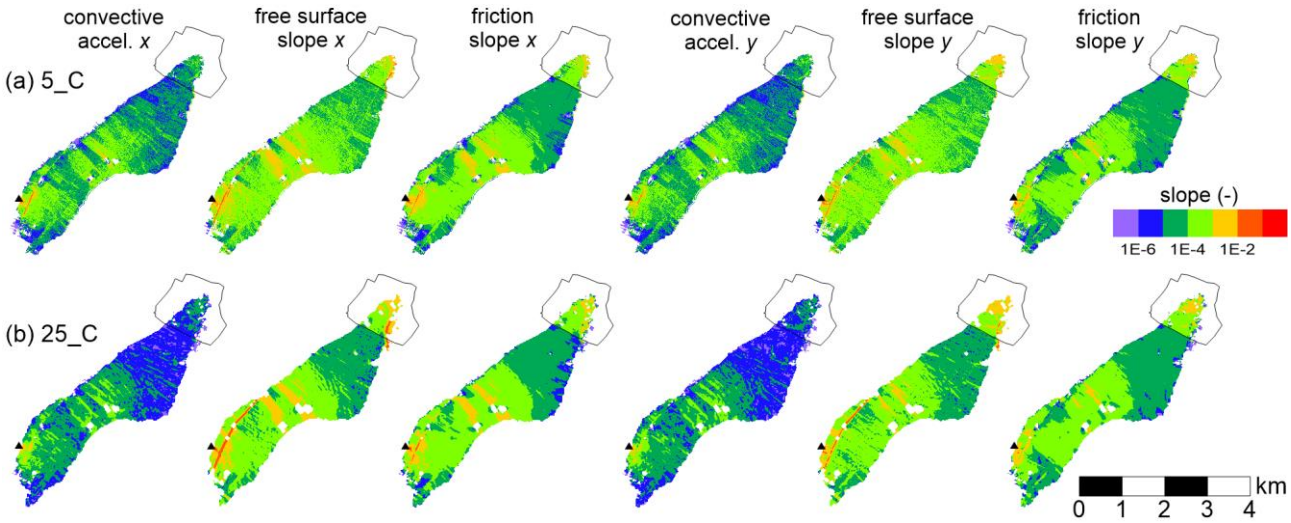

Figure 15 – Contour maps of terms (ii), (iii), and (iv) of Eq. 12 along the x and y directions for the Secchia River case study, predicted by PARFLOOD, 8 hours after the breach opening, for configurations (a) 5_C, and (b) 25_C. The black triangle identifies the breach position (inflow), and the thin line indicates the urban area of Bastiglia.

4.4 Computational times, time step size, and mass conservation

Mass conservation represents a critical point for the numerical simulation of flood propagation over an initially dry bathymetry, such as the Secchia case. We analyzed the mass balance guaranteed by the two models for this test case (with only one inflow boundary condition) for configurations 5_C, 25_C, and 50_C. The mass errors for this subset of simulations are negligible compared to the total inflow: the relative error is below 0.005% for all simulations. Since large mass conservation errors represent an indirect indicator of instabilities for LISFLOOD-FP (Neal et al., 2012b), these data also confirm that the model remains stable throughout the simulation, despite critical flows can be expected somewhere.

As mentioned earlier, the two models are characterized by different formulations of the CFL stability condition for determining the time step size during the simulations. Table 4 compares the average time step size for a subset of simulations. As expected for both models, the allowable time step increases with the grid size, because of the linear dependency between these two parameters (see Eqs. 3 and 9). However, when the same grid resolution is used, time steps of LISFLOOD-FP are 1.5-2 times larger than those of PARFLOOD: the CFL condition of the former model states the inverse proportionality of the allowable time step with the celerity of gravity waves ($\sqrt{gh}$), while the flow velocity also contributes to restrict the time step for the latter model. For both models, the Po River test case requires a smaller time step for stability compared to the Secchia test case when a similar grid size is adopted, because of the higher water levels predicted during the simulations.

Table 4 – Average time step size for some selected test cases.

Test	Average time step (s)	
Name	**PARFLOOD**	**LISFLOOD-FP**
Po 30 m	0.64	1.20
Po 50 m	1.08	2.04
Po 100 m	2.38	4.50
Secchia 5_C	0.24	0.44
Secchia 25_C	1.62	3.17
Secchia 50_C	3.68	5*

*Simulation performed with fixed time step.

The computational times required by the two models for different simulations are summarized in Table 5, together with the values of the ratio of physical to computational time R_T. The physical duration of the events here simulated is equal to 191 h and 48 h for the Po River and Secchia River test cases, respectively. As regards the Secchia test case, only runtimes for configurations 5_C, 25_C, and 50_C are reported, since similar runtimes were obtained for simulations with different roughness coefficient and equal grid size. For the simulations with the lowest resolution grid (domains with less than 10^5 cells), LISFLOOD-FP runs slightly faster than PARFLOOD; runtimes vary between less than one minute to a few minutes. Actually, it is well known that the computational capabilities of GPU-accelerated models like PARFLOOD are not fully exploited when a relatively low number of cells is processed due to the impossibility of masking the high memory latencies that characterize the GPUs (Vacondio et al., 2017). However, as the number of cells in the domain increases, PARFLOOD tends to outperform LISFLOOD-FP, despite the smaller allowable time step (Table 4) and the more complex numerical scheme, which requires more floating-point operations for a given number of cells. For the simulations with the highest spatial resolution, the former model is 2-3 times faster than the latter, with runtimes ranging from 1.5-1.8 h for PARFLOOD to almost 4 h for LISFLOOD-FP.

Incidentally, rather than by the total number of cells in the domain, runtimes are influenced by the number of wet cells in the simulation; in fact, both models are designed to skip the updating of dry cells. For the Po River test case, almost 90% of the domain is wet, while flooded cells are only up to 30% for the Secchia test case. Together with the larger allowable time step for stability (as previously discussed), this contributes to obtain larger values of R_T for the latter test case than the former, as regards simulations characterized by roughly the same total number of cells.

Table 5 – Computational times and R_T for selected test cases.

Test	N cells	Computational time (min)		R_T (-)	
Name	**($\cdot 10^6$)**	**PARFLOOD**	**LISFLOOD-FP**	**PARFLOOD**	**LISFLOOD-FP**
Po 30 m	0.91	85	232	134	49
Po 50 m	0.33	24.4	80	467	142
Po 100 m	0.09	5.1	3	2235	3800
Secchia 5_C	7.88	105	225	27	13
Secchia 25_C	0.32	1.4	1.42	2046	2017
Secchia 50_C	0.08	0.36	0.28	7958	10232

A direct comparison of the computational times of the two models using the same workstation/cluster is impossible, given the intrinsically different hardware requirements. In this work, simulations were run on high-end computational resources. However, the reported runtimes can obviously change depending on the type of processor and number of cores for LISFLOOD-FP, and on the GPU device for PARFLOOD. Just to give an idea, previous works (Neal et al., 2018) report that the computational times of LISFLOOD-FP simulations performed on 16 cores can be 4-8 times faster for 2D real test cases with ~10^4-10^5 cells, and up to 10 times faster for analytical test cases with ~10^6 cells, compared to the same runs on a single core. Here, we are using 40 cores, hence the runtimes would largely increase if a more limited number of cores were available for computation. Similarly, PARFLOOD simulations can require a longer runtime when a more "outdated" GPU is used: for example, on a NVIDIA K40 GPU (released in 2013), the "Po 50 m" test runs in 83 minutes, and test "Secchia 5_C" runs in 422 minutes. On the other hand, when a more modern video card (NVIDIA V100 GPU, released in 2017) is used, the runtimes of PARFLOOD can be reduced by roughly 25-30% (e.g. test case "Po 50 m" only takes 17 minutes to run, while test "Secchia 5_C" takes 78 minutes).

One final remark must be dedicated to the floating-point precision assumed for the computations. In this work, all simulations were run in double precision mode in order to minimize the accumulation of numerical truncation errors, which may generate non-negligible mass errors. This is nowadays the default choice for most CPU systems, while GPU processors were originally developed and optimized for single-precision computations, which can be up to eight times faster than double precision, depending on the device (Morales-Hernández et al., 2020). In this work, we verified that the runtime of single-precision simulations with PARFLOOD is roughly halved compared to double precision on modern GPUs: for example, the "Secchia 5_C" simulation runs in 55 minutes on the NVIDIA P100 GPU, and in only 36 minutes on the V100 GPU. Results are not deeply affected, and the total mass error remains acceptable (below 0.06% of the total inflow). Hence, GPU-accelerated models can be considered even more competitive for applications for which single precision can be adopted.

5. Discussion and conclusions

This work aimed at comparing two modelling strategies that have recently emerged for performing 2D large-scale flood simulations. The first one, implemented in the LISFLOOD-FP code, combines a simplification of the SWEs (i.e. local inertial approximation) and a parallelization based on OpenMP. The second approach, adopted by the PARFLOOD code, exploits the computational power of GPU devices to reduce runtimes while solving the fully dynamic SWEs. Two case studies in Italy were selected for the comparison.

Once calibrated, the two models perform similarly as regards the prediction of the inundated area and maximum water levels. This is in line with previous benchmarking studies (e.g. Néelz & Pender, 2013). The 2000 flood event on the Po River is reasonably reproduced by both models. The lowland inundation due to the Secchia levee breach is also predicted quite well.

The two models, however, require quite different values of the roughness coefficients to obtain the best results for both test cases. In particular, the calibrated values for LISFLOOD-FP are higher than the ones of PARFLOOD, especially for the Po River floodplains. Roughness also influences the flood arrival times and maximum velocities, which is evident from the results of the Secchia test case (Figure 11), where, again, LISFLOOD-FP requires higher values of Manning's coefficient to predict the correct flood arrival times, compared to PARFLOOD, in case of a high-resolution mesh. These results confirm the importance of the calibration phase (if possible, i.e., if observed data are available) for both models, and suggest that the direct adoption of any literature value based on the land use of the area is not recommended in general, since the "best" values may be model-, mesh-, and case-dependent. Indeed, roughness coefficients somehow compensate for possible inaccuracies in the terrain description (especially at coarse resolution) and, in the case of simplified models like LISFLOOD-FP, also for the reduced complexity of the governing equations. The analysis reported in Section 4.3 shows that the convective acceleration term of the SWEs can be locally non-negligible even for case studies involving gradually varied flows, and this fact probably needs to be counterbalanced by a higher friction term for LISFLOOD-FP compared to PARFLOOD. When the importance of inertial terms decreases (e.g. for the Secchia case study at coarse grid sizes), LISFLOOD-FP guarantees a good adherence to observations even when lower roughness values are considered. Incidentally, no preliminary evaluations concerning the applicability of simplified equations to the specific case study (e.g. does inertia influence the hydraulic process?) need to be carried out if the fully dynamic equations are adopted.

The influence of the grid size was also analyzed for the Secchia case study, since the use of low-resolution meshes is a common strategy to reduce computational times. However, coarse grids for raster-based models may decrease the accuracy of the terrain representation, unless suitable aggregation techniques that consider linear features are adopted. In this work, embankments were manually "burnt" into the aggregated data at all resolutions to avoid misestimating the inundated area. Thanks to this strategy, the overall accuracy at low resolutions remains fairly good for both

models, though lower than the one obtained with the high-resolution mesh. At the same time, the simulation times are largely reduced. This trade-off effect often allows practitioners to use a coarse grid size for practical applications in large-scale domains. However, the possibility of using a low resolution can sometimes be hindered by particular topographic conditions in the study area. An example is represented by the “bottleneck” of Pontelagoscuro for the Po River test case, where water levels are largely overestimated (by both models) because of the artificial flow-area “shrinkage” due to the coarse mesh.

Finally, an inter-model comparison was performed based on the computational times required for each simulation. Runtimes obviously depend on the hardware (typical HPC resources were used here), but also on the total number of cells in the domain, on the physical time of simulation, on the percentage of wet cells, and on the time step size. This latter parameter is larger for LISFLOOD-FP than PARFLOOD due to the different stability condition: this leads to a lower number of overall time steps for completing the simulation, physical time being equal. Despite this, for grids with a relatively low number of cells (~10^4-10^5), both models perform similarly, while PARFLOOD outperforms LISFLOOD-FP when the number of cells increases (~10^6), thanks to the GPU parallelization. Moreover, PARFLOOD’s runtimes can be further reduced if first-order accurate and/or single-precision simulations are performed; additionally, the upcoming new version of LISFLOOD-FP will also support GPU acceleration (Shaw et al., 2021), and multi-GPU codes with enhanced computational performance are underway (e.g. Turchetto et al., 2019; Morales-Hernández et al., 2020). In the near future, these extremely efficient codes are expected to become widely available and enable unprecedented hydraulic simulations.

In the wide context of 2D large-scale hydraulic studies, these considerations suggest that:

- for simulations that can be performed at coarse resolution and with a limited number of cells, parallelized simplified models like LISFLOOD-FP can provide similar results to fully dynamic models and comparable runtimes to GPU-accelerated codes, and represent a good alternative;
- for applications that require a higher level of detail (fine-resolution meshes with millions of cells), the adoption of reduced-complexity models is no longer justified by their computational performance compared to GPU-parallelized codes like PARFLOOD, which additionally provides reliable results in all flow conditions, including rapidly varying and supercritical flows, thanks to its fully dynamic implementation.

6. Software availability

The LISFLOOD-FP software is developed by the University of Bristol (website: http://www.bristol.ac.uk/geography/research/hydrology/models/lisflood/). The PARFLOOD code is developed by the University of Parma (website:

http://www.hylab.unipr.it/it/servizi/numerico/development-of-2d-parallel-algorithms-for-flood-propagation/). The main software specifications for both models are reported in Table 1.

Acknowledgements

The authors would like to thank the Po River Basin Authority for providing terrain data. This research benefits from the HPC facility of the University of Parma. S.D. and R.V. gratefully acknowledge the support of CINECA under project NEMORINO (ID: HP10CR41J6).

References

Afshari, S., Tavakoly, A. A., Rajib, M. A., Zheng, X., Follum, M. L., Omranian, E., & Fekete, B. M. (2018). Comparison of new generation low-complexity flood inundation mapping tools with a hydrodynamic model. Journal of Hydrology, 556, 539-556. https://doi.org/10.1016/j.jhydrol.2017.11.036

Ahmadian, R., Falconer, R. A., & Wicks, J. (2018). Benchmarking of flood inundation extent using various dynamically linked one-and two-dimensional approaches. Journal of Flood Risk Management, 11, S314-S328. https://doi.org/10.1111/jfr3.12208

Alcrudo, F., & Garcia-Navarro, P. (1993). A high-resolution Godunov-type scheme in finite volumes for the 2D shallow-water equations. International Journal for Numerical Methods in Fluids, 16(6), 489-505. https://doi.org/10.1002/fld.1650160604

Ali, A. M., Solomatine, D. P., & Di Baldassarre, G. (2015). Assessing the impact of different sources of topographic data on 1-D hydraulic modelling of floods. Hydrology and Earth System Sciences, 19(1), 631-643. https://doi.org/10.5194/hess-19-631-2015

Amadio, M., Scorzini, A. R., Carisi, F., Essenfelder, A. H., Domeneghetti, A., Mysiak, J., & Castellarin, A. (2019). Testing empirical and synthetic flood damage models: the case of Italy. Natural Hazards & Earth System Sciences, 19(3). https://doi.org/10.5194/nhess-19-661-2019

Aricò, C., Sinagra, M., Begnudelli, L., & Tucciarelli, T. (2011). MAST-2D diffusive model for flood prediction on domains with triangular Delaunay unstructured meshes. Advances in Water Resources, 34(11), 1427-1449. https://doi.org/10.1016/j.advwatres.2011.08.002

Aronica, G., Tucciarelli, T., & Nasello, C. (1998). 2D multilevel model for flood wave propagation in flood-affected areas. Journal of Water Resources Planning and Management, 124(4), 210-217. https://doi.org/10.1061/(ASCE)0733-9496(1998)124:4(210)

Arrighi, C., Pregnolato, M., Dawson, R. J., & Castelli, F. (2019). Preparedness against mobility disruption by floods. Science of the Total Environment, 654, 1010-1022. https://doi.org/10.1016/j.scitotenv.2018.11.191

Aureli, F., Maranzoni, A., Mignosa, P., & Ziveri, C. (2008). A weighted surface-depth gradient method for the numerical integration of the 2D shallow water equations with topography. Advances in Water Resources, 31(7), 962-974. https://doi.org/10.1016/j.advwatres.2008.03.005

Aureli, F., & Mignosa, P. (2004, March). Flooding scenarios due to levee breaking in the Po river. In Proceedings of the Institution of Civil Engineers-Water Management (Vol. 157, No. 1, pp. 3-12). Thomas Telford Ltd. https://doi.org/10.1680/wama.2004.157.1.3

Bates, P. D., & De Roo, A. P. J. (2000). A simple raster-based model for flood inundation simulation. Journal of Hydrology, 236(1-2), 54-77. https://doi.org/10.1016/S0022-1694(00)00278-X

Bates, P. D., Horritt, M. S., & Fewtrell, T. J. (2010). A simple inertial formulation of the shallow water equations for efficient two-dimensional flood inundation modelling. Journal of Hydrology, 387(1-2), 33-45. https://doi.org/10.1016/j.jhydrol.2010.03.027

Bates, P., Trigg, M., Neal, J., & Dabrowa, A. (2013). LISFLOOD-FP user manual. Code release, 5(6).

Bladé, E., Gómez-Valentín, M., Dolz, J., Aragón-Hernández, J. L., Corestein, G., & Sánchez-Juny, M. (2012). Integration of 1D and 2D finite volume schemes for computations of water flow in natural channels. Advances in Water Resources, 42, 17-29. https://doi.org/10.1016/j.advwatres.2012.03.021

Brunner, G. W. (2016). HEC-RAS river analysis system: hydraulic reference manual. US Army Corps of Engineers, Institute for Water Resources, Hydrologic Engineering Center.

Carisi, F., Schröter, K., Domeneghetti, A., Kreibich, H., & Castellarin, A. (2018). Development and assessment of uni-and multivariable flood loss models for Emilia-Romagna (Italy). Natural Hazards and Earth System Sciences, 18, 2057-2079. https://doi.org/10.5194/nhess-18-2057-2018

Cassardo, C., Cremonini, R., Gandini, D., Paesano, G., Pelosini, R., & Qian, M. W. (2001). Analysis of the severe flood of 13t-16th October 2000 in Piedmont (Italy). Cuadernos de Investigación Geográfica, 27, 147-162.

Castellarin, A., Di Baldassarre, G., & Brath, A. (2011). Floodplain management strategies for flood attenuation in the river Po. River Research and Applications, 27(8), 1037-1047. https://doi.org/10.1002/rra.1405

Caviedes-Voullième, D., Fernández-Pato, J., & Hinz, C. (2020). Performance assessment of 2D Zero-Inertia and Shallow Water models for simulating rainfall-runoff processes. Journal of Hydrology, 584, 124663. https://doi.org/10.1016/j.jhydrol.2020.124663

Cea, L., Garrido, M., & Puertas, J. (2010). Experimental validation of two-dimensional depth-averaged models for forecasting rainfall–runoff from precipitation data in urban areas. Journal of Hydrology, 382(1-4), 88-102. https://doi.org/10.1016/j.jhydrol.2009.12.020

Chow, V.T., Maidment, D.R., & Mays, L.W. (1988). Applied Hydrology. McGraw-Hill, New York.

Costabile, P., Costanzo, C., & Macchione, F. (2012). Comparative analysis of overland flow models using finite volume schemes. Journal of Hydroinformatics, 14(1), 122-135. https://doi.org/10.2166/hydro.2011.077

Costabile, P., Costanzo, C., & Macchione, F. (2017). Performances and limitations of the diffusive approximation of the 2-d shallow water equations for flood simulation in urban and rural areas. Applied Numerical Mathematics, 116, 141-156. https://doi.org/10.1016/j.apnum.2016.07.003

Costabile, P., Costanzo, C., De Lorenzo, G., & Macchione, F. (2020a). Is local flood hazard assessment in urban areas significantly influenced by the physical complexity of the hydrodynamic inundation model?. Journal of Hydrology, 580, 124231. https://doi.org/10.1016/j.jhydrol.2019.124231

Costabile, P., Costanzo, C., Ferraro, D., Macchione, F., & Petaccia, G. (2020b). Performances of the New HEC-RAS Version 5 for 2-D Hydrodynamic-Based Rainfall-Runoff Simulations at Basin Scale: Comparison with a State-of-the Art Model. Water, 12(9), 2326. https://doi.org/10.3390/w12092326

Coulthard, T. J., Neal, J. C., Bates, P. D., Ramirez, J., de Almeida, G. A., & Hancock, G. R. (2013). Integrating the LISFLOOD-FP 2D hydrodynamic model with the CAESAR model: implications for modelling landscape evolution. Earth Surface Processes and Landforms, 38(15), 1897-1906. https://doi.org/10.1002/esp.3478

Courty, L. G., Soriano-Monzalvo, J. C., & Pedrozo-Acuña, A. (2019). Evaluation of open-access global digital elevation models (AW3D30, SRTM, and ASTER) for flood modelling purposes. Journal of Flood Risk Management, 12, e12550. https://doi.org/10.1111/jfr3.12550

Cozzolino, L., Cimorelli, L., Della Morte, R., Pugliano, G., Piscopo, V., & Pianese, D. (2019). Flood propagation modeling with the Local Inertia Approximation: Theoretical and numerical analysis of its physical limitations. Advances in Water Resources, 133, 103422. https://doi.org/10.1016/j.advwatres.2019.103422

Cozzolino, L., Varra, G., Cimorelli, L., Pianese, D., & Della Morte, R. (2021). Friction decoupling and loss of rotational invariance in 2D flooding models. Advances in Water Resources, 152, 103919. https://doi.org/10.1016/j.advwatres.2021.103919

Cunge, J. A., Holly, F. M., & Verwey, A. (1980). Practical aspects of computational river hydraulics, Pitman Pub. Inc, London.

D'Alpaos, L., Brath, A., Fioravante, V., Gottardi, G., Mignosa, P., & Orlandini, S. (2014). Relazione tecnico-scientifica sulle cause del collasso dell'argine del fiume Secchia avvenuto il giorno 19 gennaio 2014 presso la frazione San Matteo: Regione Emilia-Romagna, Bologna (Technical-scientific report on the causes of the collapse of the bank of the Secchia River on January 19, 2014 in the San Matteo district: Emilia-Romagna Region, Bologna, in Italian).

Dazzi, S., Vacondio, R., Dal Palù, A., & Mignosa, P. (2018). A local time stepping algorithm for GPU-accelerated 2D shallow water models. Advances in Water Resources, 111, 274-288. https://doi.org/10.1016/j.advwatres.2017.11.023

Dazzi, S., Vacondio, R., & Mignosa, P. (2019). Integration of a levee breach erosion model in a GPU-accelerated 2D shallow water equations code. Water Resources Research, 55 (1), 682-702. https://doi.org/10.1029/2018WR023826

Dazzi, S., Vacondio, R., & Mignosa, P. (2020). Internal boundary conditions for a GPU-accelerated 2D shallow water model: Implementation and applications. Advances in Water Resources, 137, 103525. https://doi.org/10.1016/j.advwatres.2020.103525

De Almeida, G. A., & Bates, P. (2013). Applicability of the local inertial approximation of the shallow water equations to flood modeling. Water Resources Research, 49(8), 4833-4844. https://doi.org/10.1002/wrcr.20366

de Moel, H. D., Van Alphen, J., & Aerts, J. C. J. H. (2009). Flood maps in Europe - methods, availability and use. Natural Hazards & Earth System Sciences, 9(2). https://doi.org/10.5194/nhess-9-289-2009

DHI (2015). MIKE11 A Modelling System for Rivers and Channels - Reference Manual. DHI: Hørsholm, Denmark.

Di Baldassarre, G., & Uhlenbrook, S. (2012). Is the current flood of data enough? A treatise on research needs for the improvement of flood modelling. Hydrological Processes, 26(1), 153-158. 10.1002/hyp.8226

Domeneghetti, A., Carisi, F., Castellarin, A., & Brath, A. (2015). Evolution of flood risk over large areas: Quantitative assessment for the Po river. Journal of Hydrology, 527, 809-823. https://doi.org/10.1016/j.jhydrol.2015.05.043

D'Oria, M., Maranzoni, A., & Mazzoleni, M. (2019). Probabilistic Assessment of Flood Hazard due to Levee Breaches Using Fragility Functions. Water Resources Research, 55(11), 8740-8764. https://doi.org/10.1029/2019WR025369

Dottori, F., Di Baldassarre, G., & Todini, E. (2013). Detailed data is welcome, but with a pinch of salt: Accuracy, precision, and uncertainty in flood inundation modeling. Water Resources Research, 49, 6079-6085. https://doi.org/10.1002/wrcr.20406

Dottori, F., Martina, M. L. V., & Figueiredo, R. (2018a). A methodology for flood susceptibility and vulnerability analysis in complex flood scenarios. Journal of Flood Risk Management, 11, S632-S645. https://doi.org/10.1111/jfr3.12234

Dottori, F., Szewczyk, W., Ciscar, J. C., Zhao, F., Alfieri, L., Hirabayashi, Y., ... & Feyen, L. (2018b). Increased human and economic losses from river flooding with anthropogenic warming. Nature Climate Change, 8(9), 781-786. https://doi.org/10.1038/s41558-018-0257-z

European Commission (2007). Directive 2007/60/EC of the European Parliament and of the Council of 23 October 2007 on the assessment and management of flood risks.

Falter, D., Vorogushyn, S., Lhomme, J., Apel, H., Gouldby, B., & Merz, B. (2013). Hydraulic model evaluation for large-scale flood risk assessments. Hydrological Processes, 27(9), 1331-1340. https://doi.org/10.1002/hyp.9553

Ferrari, A., Dazzi, S., Vacondio, R., & Mignosa, P. (2020). Enhancing the resilience to flooding induced by levee breaches in lowland areas: a methodology based on numerical modelling. Natural Hazards & Earth System Sciences, 20(1). 10.5194/nhess-20-59-2020

Galland, J. C., Goutal, N., & Hervouet, J. M. (1991). TELEMAC: A new numerical model for solving shallow water equations. Advances in Water Resources, 14(3), 138-148.

Gallegos, H. A., Schubert, J. E., & Sanders, B. F. (2009). Two-dimensional, high-resolution modeling of urban dam-break flooding: A case study of Baldwin Hills, California. Advances in Water Resources, 32(8), 1323-1335. https://doi.org/10.1016/j.advwatres.2009.05.008

Horritt, M. S., & Bates, P. D. (2002). Evaluation of 1D and 2D numerical models for predicting river flood inundation. Journal of Hydrology, 268(1-4), 87-99. https://doi.org/10.1016/S0022-1694(02)00121-X

Hunter, N. M., Bates, P. D., Neelz, S., Pender, G., Villanueva, I., Wright, N. G., ... & Crossley, A. J. (2008, February). Benchmarking 2D hydraulic models for urban flooding. In Proceedings of the Institution of Civil Engineers-Water Management (Vol. 161, No. 1, pp. 13-30). Thomas Telford Ltd. https://doi.org/10.1680/wama.2008.161.1.13

Jarihani, A. A., Callow, J. N., McVicar, T. R., Van Niel, T. G., & Larsen, J. R. (2015). Satellite-derived Digital Elevation Model (DEM) selection, preparation and correction for hydrodynamic modelling in large, low-gradient and data-sparse catchments. Journal of Hydrology, 524, 489-506. https://doi.org/10.1016/j.jhydrol.2015.02.049

Klijn, F., Samuels, P., & Van Os, A. (2008). Towards flood risk management in the EU: state of affairs with examples from various European countries. International Journal of River Basin Management, 6(4), 307-321. https://doi.org/10.1080/15715124.2008.9635358

Kvočka, D., Falconer, R. A., & Bray, M. (2015). Appropriate model use for predicting elevations and inundation extent for extreme flood events. Natural Hazards, 79(3), 1791-1808. https://doi.org/10.1007/s11069-015-1926-0

Kurganov, A., & Petrova, G. (2007). A second-order well-balanced positivity preserving central-upwind scheme for the Saint-Venant system. Communications in Mathematical Sciences, 5(1), 133-160. 10.4310/CMS.2007.v5.n1.a6

Lacasta, A., Morales-Hernández, M., Murillo, J., & García-Navarro, P. (2014). An optimized GPU implementation of a 2D free surface simulation model on unstructured meshes. Advances in Engineering Software, 78, 1-15. 10.1016/j.advengsoft.2014.08.007

Lhomme, J., Sayers, P., Gouldby, B., Samuels, P., Wills, M. and Mulet-Marti, J. (2008). Recent development and application of a rapid flood spreading method. In Flood Risk Management: Research and Practice, Proceedings FLOODrisk 2008 (30 September to 2 October 2008, Oxford), edited by P. Samuels, S. Huntington, W. Allsop and J. Harrop, 15-24. Boca Raton, FL: CRC Press.

Liang, Q., & Marche, F. (2009). Numerical resolution of well-balanced shallow water equations with complex source terms. Advances in Water Resources, 32, 873-884. 10.1016/j.advwatres.2009.02.010

Luke, A., Kaplan, B., Neal, J., Lant, J., Sanders, B., Bates, P., & Alsdorf, D. (2015). Hydraulic modeling of the 2011 New Madrid Floodway activation: a case study on floodway activation controls. Natural Hazards, 77(3), 1863-1887. 10.1007/s11069-015-1680-3

Manfreda, S., Nardi, F., Samela, C., Grimaldi, S., Taramasso, A. C., Roth, G., & Sole, A. (2014). Investigation on the use of geomorphic approaches for the delineation of flood prone areas. Journal of Hydrology, 517, 863-876. https://doi.org/10.1016/j.jhydrol.2014.06.009

Marks, K., & Bates, P. (2000). Integration of high-resolution topographic data with floodplain flow models. Hydrological Processes, 14(11-12), 2109-2122. https://doi.org/10.1002/1099-1085(20000815/30)14:11/12<2109::AID-HYP58>3.0.CO;2-1

Martins, R., Leandro, J., & Djordjević, S. (2015). A well balanced Roe scheme for the local inertial equations with an unstructured mesh. Advances in Water Resources, 83, 351-363. https://doi.org/10.1016/j.advwatres.2015.07.007

Merz, B., Kreibich, H., & Lall, U. (2013). Multi-variate flood damage assessment: a tree-based data-mining approach. Natural Hazards and Earth System Sciences, 13(1), 53-64. https://doi.org/10.5194/nhess-13-53-2013

Morales-Hernández, M., García-Navarro, P., Burguete, J., & Brufau, P. (2013). A conservative strategy to couple 1D and 2D models for shallow water flow simulation. Computers & Fluids, 81, 26-44. https://doi.org/10.1016/j.compfluid.2013.04.001

Morales-Hernández, M., Sharif, M. B., Gangrade, S., Dullo, T. T., Kao, S. C., Kalyanapu, A., ... & Hodges, B. R. (2020). High-performance computing in water resources hydrodynamics. Journal of Hydroinformatics, 22(5), 1217-1235. https://doi.org/10.2166/hydro.2020.163

Morsy, M. M., Goodall, J. L., O'Neil, G. L., Sadler, J. M., Voce, D., Hassan, G., & Huxley, C. (2018). A cloud-based flood warning system for forecasting impacts to transportation infrastructure systems. Environmental Modelling & Software, 107, 231-244. https://doi.org/10.1016/j.envsoft.2018.05.007

Nardi, F., Vivoni, E. R., & Grimaldi, S. (2006). Investigating a floodplain scaling relation using a hydrogeomorphic delineation method. Water Resources Research, 42(9). https://doi.org/10.1029/2005WR004155

Neal, J., Fewtrell, T., & Trigg, M. (2009). Parallelisation of storage cell flood models using OpenMP. Environmental Modelling & Software, 24(7), 872-877. https://doi.org/10.1016/j.envsoft.2008.12.004

Neal, J. C., Fewtrell, T. J., Bates, P. D., & Wright, N. G. (2010). A comparison of three parallelisation methods for 2D flood inundation models. Environmental Modelling & Software, 25(4), 398-411. https://doi.org/10.1016/j.envsoft.2009.11.007

Neal, J., Schumann, G., & Bates, P. (2012a). A subgrid channel model for simulating river hydraulics and floodplain inundation over large and data sparse areas. Water Resources Research, 48(11). https://doi.org/10.1029/2012WR012514

Neal, J., Villanueva, I., Wright, N., Willis, T., Fewtrell, T., & Bates, P. (2012b). How much physical complexity is needed to model flood inundation?. Hydrological Processes, 26(15), 2264-2282. https://doi.org/10.1002/hyp.8339

Neal, J., Dunne, T., Sampson, C., Smith, A., & Bates, P. (2018). Optimisation of the two-dimensional hydraulic model LISFOOD-FP for CPU architecture. Environmental modelling & software, 107, 148-157. https://doi.org/10.1016/j.envsoft.2018.05.011

Néelz, S., & Pender, G. (2013). Benchmarking the latest generation of 2D hydraulic modelling packages. Report – SC120002. Environment Agency, Horison House, Deanery Road, Bristol, BS1 9AH.

Nobre, A. D., Cuartas, L. A., Momo, M. R., Severo, D. L., Pinheiro, A., & Nobre, C. A. (2016). HAND contour: a new proxy predictor of inundation extent. Hydrological Processes, 30(2), 320-333. https://doi.org/10.1002/hyp.10581

Orlandini, S., Moretti, G., & Albertson, J. D. (2015). Evidence of an emerging levee failure mechanism causing disastrous floods in Italy. Water Resources Research, 51(10), 7995-8011. https://doi.org/10.1002/2015WR017426

Paz, A. R., Bravo, J. M., Allasia, D., Collischonn, W., & Tucci, C. E. M. (2010). Large-scale hydrodynamic modeling of a complex river network and floodplains. Journal of Hydrologic Engineering, 15(2), 152-165. https://doi.org/10.1061/(ASCE)HE.1943-5584.0000162

Pinter, N., Huthoff, F., Dierauer, J., Remo, J. W., & Damptz, A. (2016). Modeling residual flood risk behind levees, Upper Mississippi River, USA. Environmental Science & Policy, 58, 131-140. https://doi.org/10.1016/j.envsci.2016.01.003

Prestininzi, P. (2008). Suitability of the diffusive model for dam break simulation: Application to a CADAM experiment. Journal of Hydrology, 361(1-2), 172-185. https://doi.org/10.1016/j.jhydrol.2008.07.050

Samela, C., Troy, T. J., & Manfreda, S. (2017). Geomorphic classifiers for flood-prone areas delineation for data-scarce environments. Advances in Water Resources, 102, 13-28. https://doi.org/10.1016/j.advwatres.2017.01.007

Sanders, B. F. (2007). Evaluation of on-line DEMs for flood inundation modeling. Advances in Water Resources, 30(8), 1831-1843. https://doi.org/10.1016/j.advwatres.2007.02.005

Sanders, B. F., Schubert, J. E., & Detwiler, R. L. (2010). ParBreZo: A parallel, unstructured grid, Godunov-type, shallow-water code for high-resolution flood inundation modeling at the regional scale. Advances in Water Resources, 33(12), 1456-1467. https://doi.org/10.1016/j.advwatres.2010.07.007

Sanders, B. F., & Schubert, J. E. (2019). PRIMo: Parallel raster inundation model. Advances in Water Resources, 126, 79-95. https://doi.org/10.1016/j.advwatres.2019.02.007

Sangireddy, H., Stark, C. P., Kladzyk, A., & Passalacqua, P. (2016). GeoNet: An open source software for the automatic and objective extraction of channel heads, channel network, and channel morphology from high resolution topography data. Environmental Modelling & Software, 83, 58-73. https://doi.org/10.1016/j.envsoft.2016.04.026

Savage, J. T. S., Pianosi, F., Bates, P., Freer, J., & Wagener, T. (2016a). Quantifying the importance of spatial resolution and other factors through global sensitivity analysis of a flood inundation model. Water Resources Research, 52(11), 9146-9163. https://doi.org/10.1002/2015WR018198

Savage, J. T. S., Bates, P., Freer, J., Neal, J., & Aronica, G. (2016b). When does spatial resolution become spurious in probabilistic flood inundation predictions?. Hydrological Processes, 30(13), 2014-2032. https://doi.org/10.1002/hyp.10749

Schubert, J. E., Burns, M. J., Fletcher, T. D., & Sanders, B. F. (2017). A framework for the case-specific assessment of Green Infrastructure in mitigating urban flood hazards. Advances in Water Resources, 108, 55-68. https://doi.org/10.1016/j.advwatres.2017.07.009

Schumann, G., Di Baldassarre, G., Alsdorf, D., & Bates, P. D. (2010). Near real-time flood wave approximation on large rivers from space: Application to the River Po, Italy. Water Resources Research, 46(5). https://doi.org/10.1029/2008WR007672

Schumann, G. J. P., Stampoulis, D., Smith, A. M., Sampson, C. C., Andreadis, K. M., Neal, J. C., & Bates, P. D. (2016). Rethinking flood hazard at the global scale. Geophysical Research Letters, 43(19), 10-249. https://doi.org/10.1002/2016GL070260

Shaw, J., Kesserwani, G., Neal, J., Bates, P., & Sharifian, M. K. (2021). LISFLOOD-FP 8.0: the new discontinuous Galerkin shallow-water solver for multi-core CPUs and GPUs. Geoscientific Model Development, 14(6), 3577-3602. https://doi.org/10.5194/gmd-14-3577-2021

Shustikova, I., Domeneghetti, A., Neal, J. C., Bates, P., & Castellarin, A. (2019). Comparing 2D capabilities of HEC-RAS and LISFLOOD-FP on complex topography. Hydrological Sciences Journal, 64(14), 1769-1782. https://doi.org/10.1080/02626667.2019.1671982

Shustikova, I., Neal, J. C., Domeneghetti, A., Bates, P. D., Vorogushyn, S., & Castellarin, A. (2020). Levee Breaching: A New Extension to the LISFLOOD-FP Model. Water, 12(4), 942. https://doi.org/10.3390/w12040942

Sofia, G., Fontana, G. D., & Tarolli, P. (2014). High-resolution topography and anthropogenic feature extraction: testing geomorphometric parameters in floodplains. Hydrological Processes, 28(4), 2046-2061. https://doi.org/10.1002/hyp.9727

Tavares da Costa, R., Manfreda, S., Luzzi, V., Samela, C., Mazzoli, P., Castellarin, A., & Bagli, S. (2019). A web application for hydrogeomorphic flood hazard mapping. Environmental Modelling & Software, 118, 172-186. https://doi.org/10.1016/j.envsoft.2019.04.010

Tavares da Costa, R., Zanardo, S., Bagli, S., Hilberts, A. G., Manfreda, S., Samela, C., & Castellarin, A. (2020). Predictive Modeling of Envelope Flood Extents Using Geomorphic and Climatic-Hydrologic Catchment Characteristics. Water Resources Research, 56(9), e2019WR026453. https://doi.org/10.1029/2019WR026453

Tayefi, V., Lane, S. N., Hardy, R. J., & Yu, D. (2007). A comparison of one-and two-dimensional approaches to modelling flood inundation over complex upland floodplains. Hydrological Processes: An International Journal, 21(23), 3190-3202. https://doi.org/10.1002/hyp.6523

Teng, J., Jakeman, A. J., Vaze, J., Croke, B. F., Dutta, D., & Kim, S. (2017). Flood inundation modelling: A review of methods, recent advances and uncertainty analysis. Environmental Modelling & Software, 90, 201-216. https://doi.org/10.1016/j.envsoft.2017.01.006

Teng, J., Vaze, J., Kim, S., Dutta, D., Jakeman, A. J., & Croke, B. F. W. (2019). Enhancing the Capability of a Simple, Computationally Efficient, Conceptual Flood Inundation Model in Hydrologically Complex Terrain. Water Resources Management, 33(2), 831-845. https://doi.org/10.1007/s11269-018-2146-7

Toro, E. (2001). Shock capturing methods for free surface shallow water flows. Wiley, Chichester, UK.

Turchetto, M., Dal Palù, A., & Vacondio, R. (2019). A general design for a scalable MPI-GPU multi-resolution 2D numerical solver. IEEE Transactions on Parallel and Distributed Systems, 31(5), 1036-1047. 10.1109/TPDS.2019.2961909

Vacondio, R., Dal Palù, A., & Mignosa, P. (2014). GPU-enhanced Finite Volume Shallow Water solver for fast flood simulations. Environmental Modelling & Software, 57, 60-75. 10.1016/j.envsoft.2014.02.003

Vacondio, R., Aureli, F., Ferrari, A., Mignosa, P., & Dal Palù, A. (2016). Simulation of the January 2014 flood on the Secchia river using a fast and high-resolution 2D parallel shallow-water numerical scheme. Natural Hazards, 80 (1), 103-125. 10.1007/s11069-015-1959-4

Vacondio, R., Dal Palù, A., Ferrari, A., Mignosa, P., Aureli, F., & Dazzi, S. (2017). A non- uniform efficient grid type for GPU-parallel shallow water equations models. Environmental Modelling & Software, 88, 119-137. 137. 10.1016/j.envsoft.2016.11.012

Winsemius, H. C., Aerts, J. C., Van Beek, L. P., Bierkens, M. F., Bouwman, A., Jongman, B., ... & Ward, P. J. (2016). Global drivers of future river flood risk. Nature Climate Change, 6(4), 381-385. https://doi.org/10.1038/nclimate2893

Vorogushyn, S., Merz, B., Lindenschmidt, K. E., & Apel, H. (2010). A new methodology for flood hazard assessment considering dike breaches. Water Resources Research, 46(8). https://doi.org/10.1029/2009WR008475

Willis, T., Wright, N., & Sleigh, A. (2019). Systematic analysis of uncertainty in 2D flood inundation models. Environmental Modelling & Software, 122, 104520. https://doi.org/10.1016/j.envsoft.2019.104520

Wing, O. E., Bates, P. D., Sampson, C. C., Smith, A. M., Johnson, K. A., & Erickson, T. A. (2017). Validation of a 30 m resolution flood hazard model of the conterminous United States. Water Resources Research, 53(9), 7968-7986. https://doi.org/10.1002/2017WR020917

Wing, O. E., Sampson, C. C., Bates, P. D., Quinn, N., Smith, A. M., & Neal, J. C. (2019a). A flood inundation forecast of Hurricane Harvey using a continental-scale 2D hydrodynamic model. Journal of Hydrology X, 4, 100039. https://doi.org/10.1016/j.hydroa.2019.100039

Wing, O. E., Bates, P. D., Neal, J. C., Sampson, C. C., Smith, A. M., Quinn, N., ... & Krajewski, W. F. (2019b). A new automated method for improved flood defense representation in large-scale hydraulic models. Water Resources Research, 55(12), 11007-11034. https://doi.org/10.1029/2019WR025957

Yan, K., Di Baldassarre, G., & Solomatine, D. P. (2013). Exploring the potential of SRTM topographic data for flood inundation modelling under uncertainty. Journal of Hydroinformatics, 15(3), 849-861. https://doi.org/10.2166/hydro.2013.137

Yu, D., & Lane, S. N. (2006). Urban fluvial flood modelling using a two-dimensional diffusion-wave treatment, part 2: development of a sub-grid-scale treatment. Hydrological Processes: An International Journal, 20(7), 1567-1583. https://doi.org/10.1002/hyp.5936

Zheng, X., Maidment, D. R., Tarboton, D. G., Liu, Y. Y., & Passalacqua, P. (2018). GeoFlood: Large-Scale Flood Inundation Mapping Based on High-Resolution Terrain Analysis. Water Resources Research, 54(12), 10-013. https://doi.org/10.1029/2018WR023457